

The global ionosphere–thermosphere model

A.J. Ridley*, Y. Deng, G. Tóth

Department of Atmosphere, Oceanic and Space Sciences, University of Michigan, Ann Arbor, MI, 48109-2143, USA

Received 3 June 2005; received in revised form 22 December 2005; accepted 3 January 2006

Available online 13 March 2006

Abstract

The recently created global ionosphere–thermosphere model (GITM) is presented. GITM uses a three-dimensional spherical grid that can be stretched in both latitude and altitude, while having a fixed resolution in longitude. GITM is nontraditional in that it does not use a pressure-based coordinate system. Instead it uses an altitude-based grid and does not assume a hydrostatic solution. This allows the model to more realistically capture physics in the high-latitude region, where auroral heating is prevalent. The code can be run in a one-dimensional (1-D) or three-dimensional (3-D) mode. In 3-D mode, the modeling region is broken into blocks of equal size for parallelization. In 1-D mode, a single latitude and longitude is modeled by neglecting any horizontal transport or gradients, except in the ionospheric potential. GITM includes a modern advection solver and realistic source terms for the continuity, momentum, and energy equations. Each neutral species has a separate vertical velocity, with coupling of the velocities through a frictional term. The ion momentum equation is solved for assuming steady-state, taking into account the pressure, gravity, neutral winds, and external electric fields. GITM is an extremely flexible code—allowing different models of high-latitude electric fields, auroral particle precipitation, solar EUV inputs, and particle energy deposition to be used. The magnetic field can be represented by an ideal dipole magnetic field or a realistic APEX magnetic field. Many of the source terms can be controlled (switched on and off, or values set) by an easily readable input file. The initial state can be set in three different ways: (1) using an ideal atmosphere, where the user inputs the densities and temperature at the bottom of the atmosphere; (2) using MSIS and IRI; and (3) restarting from a previous run. A 3-D equinox run and a 3-D northern summer solstice run are presented. These simulations are compared with MSIS and IRI to show that the large-scale features are reproduced within the code. We conduct a second equinox simulation with different initial conditions to show that the runs converge after approximately 1.5 days. Additionally, a 1-D simulation is presented to show that GITM works in 1-D and that the dynamics are what is expected for such a model.

© 2006 Elsevier Ltd. All rights reserved.

Keywords: Thermosphere; Ionosphere; Modeling; Global circulation models

1. Introduction

An understanding of both the thermosphere and the ionosphere, two tightly coupled, overlapping

regions of the atmosphere, is important for a number of research and space weather applications, for example: (1) examining increased satellite drag due to heating of the atmosphere; (2) examining where and when strong gradients of total electron content will occur for GPS signal degradation analysis; (3) determining when and where high frequency signals will be strongly scattered or lost

*Corresponding author. Tel.: +1 734 764 5727;
fax: +1 734 647 3083.

E-mail address: ridley@umich.edu (A.J. Ridley).

due to ionospheric scintillation; (4) examining the role of ionospheric and thermospheric dynamics on the climatology of the lower atmosphere; and (5) determining how the ionosphere influences the magnetosphere through ionospheric conductance and outflow. These issues can be examined by the use of large-scale data systems or through the use of global or localized thermosphere and ionosphere models.

One of the most important descriptions of the thermospheric region is MSIS (Hedin, 1983, 1987, 1991). MSIS is an empirical model that relates the neutral densities and temperature to the integrated solar flux approximation ($F_{10.7}$) and activity level (A_p). It is a spherical harmonic fit to many different satellite and remote observations. The description is based on a large amount of data, and therefore it is felt that it represents the average conditions for the given inputs. MSIS has been improved by adding time dependence, allowing storm periods to be modeled more accurately.

The international reference ionosphere (IRI) is similar to MSIS, but for the ionosphere (Rawer et al., 1978; Bilitza, 2001). It models the ionospheric density and temperatures for all latitudes and local times, but does not include any auroral precipitation, which makes the model unrealistic in the auroral regions for medium and strong auroral activity.

In order to actually examine how the neutrals and ions are coupled together, one needs to turn to more sophisticated models of the coupled system. First-principles based models simulate the thermosphere and ionosphere by determining the density, momentum, and energy self-consistently. One of the first global models of this type was the thermosphere general circulation model (TGCM) (Dickinson et al., 1981, 1984). This model used an empirical ionosphere to drive the chemistry and dynamics of the thermosphere. The TGCM (and its later variants) solve for mass mixing ratios of the neutral major species O_2 , N_2 , and O and the minor species $N(^2D)$, $N(^4S)$, NO , He , and Ar , and is a full three-dimensional (3-D) code with 5° latitude by 5° longitude by 0.5 scale height altitude cells. There are 29 pressure levels in the vertical direction such that the computational domain spans from ~ 95 km to 650 km in altitude. The second model of this line includes a self-consistent ionosphere (TIGCM) (Roble et al., 1988). Within the TIGCM the O^+ dynamics are considered, while the species O_2^+ , N_2^+ , NO^+ , and N^+ are assumed to be in photochemical

equilibrium. This model includes an auroral precipitation model with empirical ionization profiles for the given precipitation energies (Roble and Ridley, 1987). In addition to the main oval, a polar cap and a spatially limited cusp precipitation are specified. These patterns are used to generate 3-D ionization rates, and therefore strongly control the electron density at high latitudes. At the high latitudes, an external electric field is assumed (Heelis et al., 1982; Richmond and Kamide, 1988), which affects the neutral dynamics through ion drag and Joule heating, but is not influenced by the ionospheric wind dynamo.

Richmond et al. (1992) added a self-consistent low-latitude electrodynamics to the TIGCM, resulting in the TIEGCM. The electrodynamics within the TIEGCM focuses on the middle and lower latitudes, with a self-consistent calculation of the interaction between the neutral winds, currents, and electric fields. A transition region exists where the model linearly scales the electric field between the high and middle latitude regions. This transition region is $\sim 10^\circ$ wide and is centered near 60° magnetic latitude. The electrodynamics of the TIEGCM are solved on a magnetic apex grid based on the 1985 International Geomagnetic Reference Field (IGRF, Richmond, 1995). Roble and Ridley (1994) extended the model down into the mesosphere (the TIMEGCM). This model added a large amount of chemistry and added OH as a main constituent within the neutral dynamics routines.

The thermosphere ionosphere nested grid (TING) model uses the TIGCM as a base, but adds a nested grid within the domain to allow for 3 times higher resolution in a limited area (Wang et al., 1999, 2001). This subgridding is typically confined to the northern auroral region, and allows the sophistication of the TGCM class of models with the higher resolution needed to start to resolve the complex structures in the high-latitude thermosphere and ionosphere. A limitation of the TING model is that the high-resolution region does not feed back to the lower resolution model.

A different first principles model is the Coupled Thermosphere Ionosphere Model (CTIM) (Fuller-Rowell and Rees, 1980, 1983; Rees and Fuller-Rowell, 1988, 1990). Recently, this model was extended to include the plasmasphere, called the Coupled Thermosphere Ionosphere Plasmasphere (CTIP) by modeling the ionosphere along field-lines, improving the mass flow between hemispheres and the upper boundary condition on the ion flow.

The thermospheric model simulates the time-dependent structure of the wind vectors, temperature and density of the neutral thermosphere with a resolution of 2° (latitude) by 18° (longitude). CTIP uses a pressure-based coordinate system, similar to the TIEGCM. A time-dependent mean mass equation was incorporated into the model by Fuller-Rowell and Rees (1983). This formalism assumes the upper atmosphere could be approximated by two species, atomic oxygen and the sum of molecular nitrogen and oxygen. The major species composition was later improved to include major species, O, O₂ and N₂, with chemistry, transport and the mutual diffusion between species. The plasmasphere component of the CTIP model adopts an Eulerian framework in which individual flux-tubes are fixed in space. The mid- and low-latitude electric fields are computed self-consistently within the model using the model of Richmond and Roble (1987).

The Coupled Middle Atmosphere and Thermosphere (CMAT) general circulation model (Harris et al., 2002) is an extension of the University College London time dependent three-dimensional CTIP model. It covers a vertical range from 10 mbar (30 km) to 7.587 pbar (300–600 km). In order to simulate mesospheric energetics, dynamics and composition, CMAT updates and extends the original thermospheric scheme. The resolution is a third scale height vertical, 2° latitude and an 18° longitude. Thermospheric heating, photodissociation and photoionization are calculated due to the absorption of solar X-ray, EUV and UV radiation between 0.1 and 194 nm. A full mesosphere-thermosphere neutral chemical scheme is included. A Hybrid Matsuno-Lindzen parameterization (Meyer, 1999) is used to calculate gravity wave drag. Lower boundary seasonal forcing is from MSIS-E90 (Hedin, 1991) and lower boundary tidal forcing from global scale wave model output.

The Global Assimilation of Ionospheric Measurements (GAIM) (Schunk et al., 2004) uses a time-dependent physics-based model of the global ionosphere-plasmasphere and a Kalman filter as a basis for assimilating a diverse set of real-time (or near real-time) measurements. GAIM will provide both specifications and forecasts on a spatial grid that can be global, regional, or local. The primary output of GAIM will be a continuous reconstruction of the three-dimensional electron density distribution from 90 km to 35,000 km. However, GAIM will also provide a range of auxiliary parameters as well as the main ionospheric drivers.

In its specification mode, GAIM will give quantitative estimates for the accuracy of the reconstructed ionospheric densities. Also, GAIM will have a modular construction, so that when new models, observing stations, and data types become available, they can be easily incorporated into the data assimilation scheme. The overall program involves model construction, data quality assessment, data assimilation, the construction of an executive system to automatically run GAIM in real time, and validation.

First-principles based models give the possibility for an improved understanding of the coupled thermosphere-ionosphere system. For example, the study presented by Killeen and Roble (1984) showed how valuable of a tool global models can be. They examined the influence of various forcing terms on the thermospheric neutral winds at various altitudes, and quantified the magnitude of different acceleration terms on the neutral wind forcing.

In this study we present a new Global Ionosphere Thermosphere Model (GITM). It differs from the above models in several respects. Some of the more important features of GITM are: adjustable resolution; non-uniform grid in the altitude and latitude coordinates; the dynamics equations are solved without the assumption of hydrostatic equilibrium; the advection is solved for explicitly, so the time-step in GITM is approximately 2–4 s; the chemistry is solved for explicitly, so there are no approximations of local chemical equilibrium; the ability to choose different models of electric fields and particle precipitation patterns; the ability to start from MSIS and IRI solutions; and the ability to use a realistic (or ideal) magnetic field determined at the time of the model run. We present the physics, chemistry, and dynamics of the model and two examples of simulation results to show that the model produces a realistic atmosphere.

2. Model description

GITM is a three-dimensional spherical code that models the Earth's thermosphere and ionosphere system using a stretched grid in latitude and altitude. In addition, the number of grid points in each direction can be specified, so the resolution is extremely flexible. GITM explicitly solves for the neutral densities of O, O₂, N(²D), N(²P), N(⁴S), N₂, NO, H, and He; and ion species O⁺(⁴S), O⁺(²D), O⁺(²P), O₂⁺, N⁺, N₂⁺, NO⁺, H⁺, and He⁺. One major difference between GITM and other

thermosphere codes is the use of an altitude grid instead of a pressure grid. The altitude spacing is done automatically using scale-heights and specifying a lower and upper boundary and the number of grid points. Fig. 1 shows examples of two altitude grids during solar minimum and maximum conditions. The vertical grid spacing is less than 3 km in the lower thermosphere, and over 10 km in the upper thermosphere. There is no longitude stretching, so the east-west spacing is simply 360° divided by the number of points in longitude. The latitude stretching is done through the use of weights which specify the location of the most (or least) dense grid points and the degree of stretching. Fig. 2 shows two example grids to demonstrate the flexibility of the horizontal grid structure.

The model is fully parallel using a block-based two-dimensional domain decomposition with latitudinal and longitudinal ghost-cells bordering the blocks (Oehmke and Stout, 2001; Oehmke, 2004). This allows parallel computation over the entire domain, exchanging information only between each iteration. GITM uses the Message Passing Interface (MPI) standard to allow for platform independence. It has been run on up to 80 processors with a resolution as fine as 1.25° latitude by 5° longitude uniform over the whole globe and 40 vertical levels.

The simulations can be initiated using MSIS and IRI neutral and ion densities and temperatures for the given date and time. For more theoretical simulations, the code can be initiated with each latitude and longitude having the same height profile from MSIS and IRI. This way, tests of how long the system takes to heat up and reach some sort of steady-state can be conducted. GITM can be restarted from a previous run, so simulations of very long time periods can be conducted without any break in the physics. Having the ability to both restart and start from a base state allows maximum flexibility in the usefulness of the code.

The model can use a dipole or the IGRF magnetic field with the APEX coordinate system (Richmond, 1995). This allows experiments ranging from highly idealized magnetic field topological cases to realistic magnetic field cases. The IGRF magnetic field can be exchanged with other systems, so simulations of paleomagnetic conditions could be examined, for example. GITM solves the non-hydrostatic equations, so it can model problems where the hydrostatic approximation is not accurate.

GITM can run in 1-D as well as 3-D. One-dimensional simulations can be carried out very

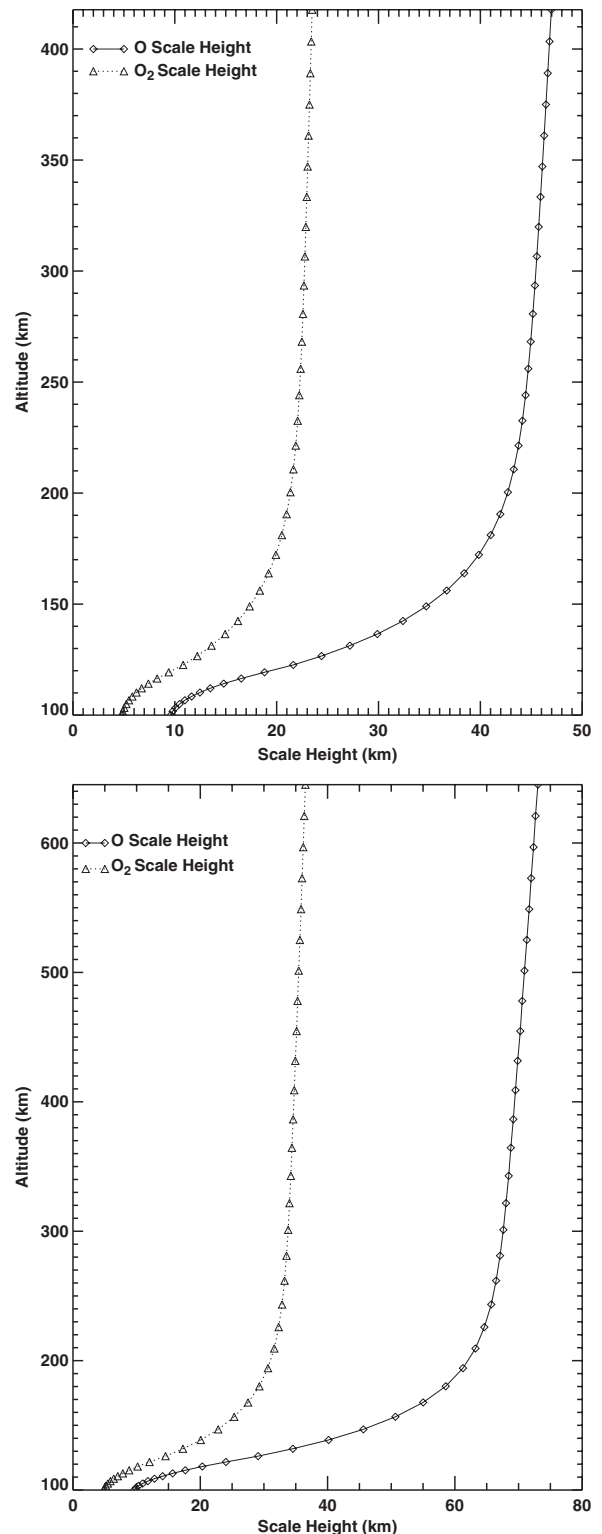


Fig. 1. Plots of the molecular and atomic oxygen scale height for runs with an $F_{10.7}$ of 100 (top) and 300 (bottom). These runs both have 40 grid points in the vertical direction and 0.3 total scale height resolution. The vertical grid points are indicated by the diamonds and triangles.

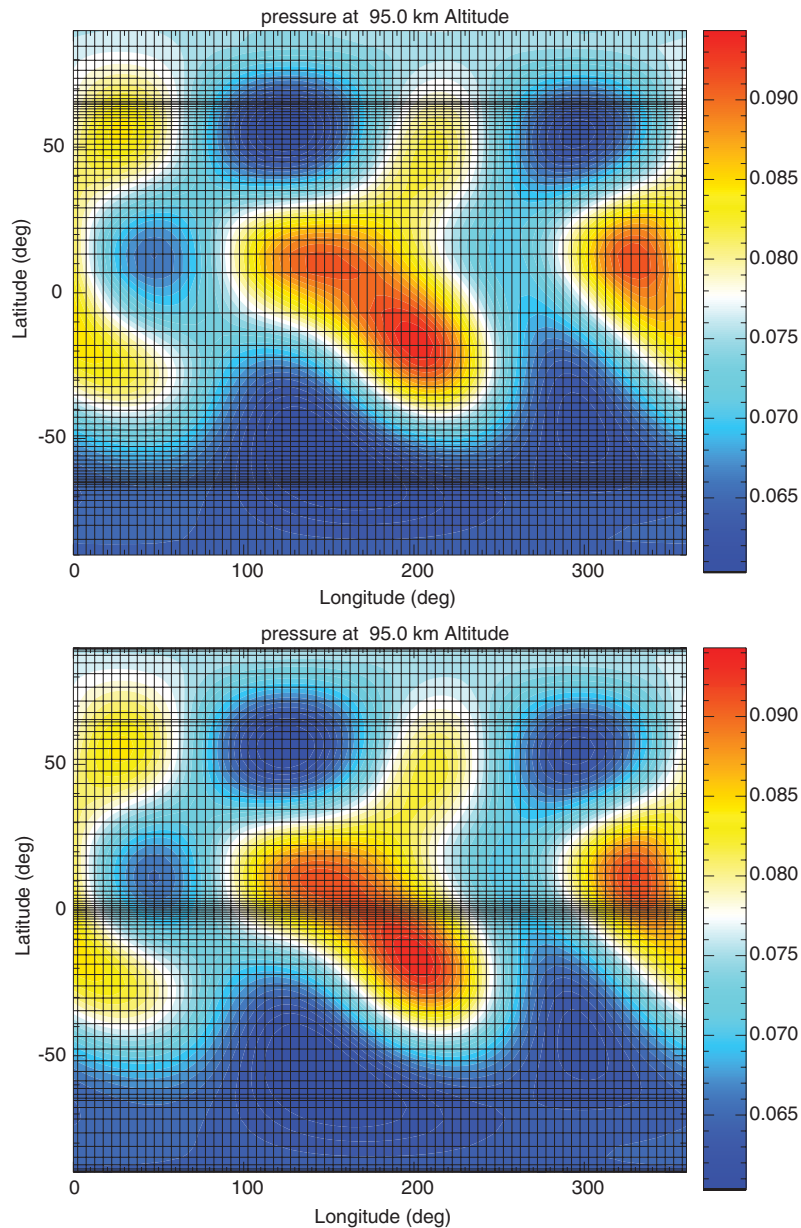


Fig. 2. Examples for the possibilities of the grid stretching in GITM. The top panel shows a possible stretched grid in which the auroral zones are highly refined, while the bottom panel shows a grid which is concentrated near the equator, auroral zones, and near the poles. The pressure (in Pascals) is shown as the contour.

efficiently on a personal computer. This allows for investigating long time periods to determine the stability of the code, and to test new physics quickly. When run in 1-D, the horizontal transport is ignored and only the vertical advection is taken into account. Full 3-D source terms are included, though, so processes such as ion drag are still taken into account. Terms that are self-consistently calculated in GITM, such as the pressure, are

considered to have no gradient in the horizontal direction. Other external driving terms, such as the electric potential are specified on a 1° by 1° grid surrounding the 1-D domain. An electric field can then be derived at the cell center, driving the horizontal ion velocities. The horizontal ion flows cause horizontal neutral winds to develop and Joule heating to occur. This feature of the model is demonstrated in section 5.

GITM is coupled to a large number of models of the high-latitude ionospheric electrodynamics. For example, we can run GITM using results from the Assimilative Mapping of Ionospheric electrodynamics (AMIE) technique (Richmond and Kamide, 1988; Richmond, 1992) as high-latitude drivers in realistic, highly dynamic time periods. We can also use the Weimer (1996), Foster (1983), Heppner and Maynard (1987) or Ridley et al. (2000) electrodynamic potential patterns and the Hardy et al. (1987) or Fuller-Rowell and Evans (1987) particle precipitation patterns for more idealized conditions. GITM is also part of the University of Michigan's Space Weather Modeling Framework (Tóth et al., 2005), so it can be coupled with a global magnetohydrodynamic (MHD) model (Powell et al., 1999) of the magnetosphere. This allows investigation of the coupling between the thermosphere–ionosphere and the magnetosphere systems (e.g. Ridley et al., 2003).

2.1. Neutral dynamics

GITM solves in altitude coordinates, and does not assume hydrostatic equilibrium, therefore the vertical solver is different than most other thermospheric codes. The exponential stratified atmosphere is difficult to solve for because the vertical gradients are quite strong. We have addressed this problem by splitting the vertical and horizontal advection. After the advection is completed, source terms (e.g., Joule heating, chemical sources and losses, viscosity, etc.) are added.

In the horizontal direction we use the total mass density ρ and number densities N_s of the individual species, where s is the index of the particular species. The mass density is the sum of the species densities:

$$\rho = \sum_s M_s N_s, \quad (1)$$

where M_s is the molecular mass of species s . In the horizontal direction all of the neutral species are assumed to move with the same velocity. We introduce a normalized neutral temperature

$$\mathcal{T} = p/\rho, \quad (2)$$

where p is the total neutral pressure. Using these variables the continuity equation is

$$\frac{\partial N_s}{\partial t} + N_s \nabla \cdot \mathbf{u} + \mathbf{u} \cdot \nabla N_s = 0, \quad (3)$$

where \mathbf{u} is the neutral velocity and t is time. The momentum equation is

$$\frac{\partial \mathbf{u}}{\partial t} + \mathbf{u} \cdot \nabla \mathbf{u} + \nabla \mathcal{T} + \frac{\mathcal{T}}{\rho} \nabla \rho = 0, \quad (4)$$

and the energy equation can be written as

$$\frac{\partial \mathcal{T}}{\partial t} + \mathbf{u} \cdot \nabla \mathcal{T} + (\gamma - 1) \mathcal{T} \nabla \cdot \mathbf{u} = 0, \quad (5)$$

where γ is the ratio of specific heats ($\frac{5}{3}$). For the horizontal advection we take the horizontal part of the above equations, i.e. the terms containing vertical derivatives are ignored.

In the vertical (or radial) direction the natural logarithm of the total mass density ρ and number densities N_s are used as the primitive variables:

$$\mathcal{R} = \ln(\rho), \quad (6)$$

$$\mathcal{N}_s = \ln(N_s). \quad (7)$$

While the density varies exponentially with height, the logarithm of density varies linearly, which is much easier to handle numerically. For the same reason we write the energy equation in terms of the normalized temperature \mathcal{T} instead of the exponentially varying p .

In the thermosphere, the neutrals can be treated as having individual vertical velocities \mathbf{u}_s . This is because above about 120 km altitude, the turbulent mixing becomes very small, and the individual species start to become hydrostatically balanced, instead of all the species having the same hydrostatic fall off. In these variables, the continuity equation for each species thus becomes

$$\frac{\partial \mathcal{N}_s}{\partial t} + \nabla \cdot \mathbf{u}_s + \mathbf{u}_s \cdot \nabla \mathcal{N}_s = 0. \quad (8)$$

The momentum equations for the species are

$$\frac{\partial \mathbf{u}_s}{\partial t} + \mathbf{u}_s \cdot \nabla \mathbf{u}_s + \frac{k}{M_s} \nabla T + \frac{k}{M_s} T \nabla \mathcal{N}_s = 0, \quad (9)$$

where

$$T = \frac{\bar{m}_n}{k} \mathcal{T} \quad (10)$$

is the un-normalized temperature. The number density weighted average mass is denoted as \bar{m}_n . In the temperature equation, the average velocity \mathbf{u} is used, which is calculated from the species velocities as

$$\mathbf{u} = \frac{1}{\rho} \sum_s M_s N_s \mathbf{u}_s. \quad (11)$$

The vertical part of Eq. (5) completes the basic equations of advection in the vertical direction. The equations need to be recast into rotating spherical coordinates and source terms need to be added.

For each species the vertical continuity equation becomes

$$\frac{\partial \mathcal{N}_s}{\partial t} + \frac{\partial u_{r,s}}{\partial r} + \frac{2u_{r,s}}{r} + u_{r,s} \frac{\partial \mathcal{N}_s}{\partial r} = \frac{1}{N_s} \mathcal{S}_s, \quad (12)$$

where r is the radial distance measured from the center of the Earth, and the subscript r denotes the radial component, therefore $u_{r,s}$ is the radial (vertical) velocity of species s . The $2u_{r,s}/r$ term comes from the radial divergence of the radial component of the velocity. The source term \mathcal{S}_s for the neutral density of species s includes the eddy diffusion and chemical sources and losses:

$$\mathcal{S}_s = \frac{\partial}{\partial r} \left[N_s K_e \left(\frac{\partial N_s}{\partial r} - \frac{\partial N}{\partial r} \right) \right] + C_s, \quad (13)$$

where K_e is the eddy diffusion coefficient, N is the total number density and C_s are the source/losses due to the chemical reactions. The chemistry within GITM will be discussed below.

In rotating spherical coordinates the vertical momentum equation becomes

$$\begin{aligned} \frac{\partial u_{r,s}}{\partial t} + u_{r,s} \frac{\partial u_{r,s}}{\partial r} + \frac{u_\theta}{r} \frac{\partial u_{r,s}}{\partial \theta} + \frac{u_\phi}{r \cos(\theta)} \frac{\partial u_{r,s}}{\partial \phi} \\ + \frac{k}{M_s} \frac{\partial T}{\partial r} + T \frac{k}{M_s} \frac{\partial \mathcal{N}_s}{\partial r} \\ = g + \mathcal{F}_s + \frac{u_\theta^2 + u_\phi^2}{r} \\ + \cos^2(\theta) \Omega^2 r + 2 \cos(\theta) \Omega u_\phi, \end{aligned} \quad (14)$$

where θ is the north latitude, ϕ is east longitude, u_θ is the northward neutral velocity, u_ϕ is the eastward neutral velocity, Ω is the angular velocity of the planet, g is gravity, and \mathcal{F}_s contains the forces due to ion-neutral and neutral-neutral friction. The last two terms are the centrifugal and Coriolis forces. The $(u_\theta^2 + u_\phi^2)/r$ term is due to the spherical geometry: the horizontal winds attempt to ‘lift off’ from the curved surface of the Earth. These three terms vanish if $\Omega = 0$ and there is no horizontal wind, and they cancel each other if $u_\phi = -r\Omega \cos(\theta)$ and $u_\theta = 0$, i.e. the wind is not rotating with the Earth.

The remaining force term is the ion-drag (Rees, 1989) and the neutral-neutral friction in the vertical

direction (Colegrove et al., 1966):

$$\mathcal{F}_s = \frac{\rho_i}{\rho_s} v_{in} (v_r - u_{r,s}) + \frac{kT}{M_s} \sum_{q \neq s} \frac{N_q}{ND_{qs}} (u_{r,q} - u_{r,s}), \quad (15)$$

where v_r is the radial component of the ion velocity, ρ_i is the ion mass density, v_{in} is the ion-neutral collision frequency, $u_{r,q}$ indicates the vertical velocity of the other constituents, and D_{qs} is the diffusion coefficient between the s and q constituents (Colegrove et al., 1966, Table 1).

The vertical temperature equation becomes

$$\frac{\partial \mathcal{T}}{\partial t} + u_r \frac{\partial \mathcal{T}}{\partial r} + (\gamma - 1) \mathcal{T} \left(\frac{2u_r}{r} + \frac{\partial u_r}{\partial r} \right) = \frac{k}{c_v \rho \bar{m}_n} \mathcal{Q}, \quad (16)$$

where the $2u_r/r$ term is once again due to the divergence of the radial velocity. The specific heat at constant volume is denoted by c_v , and is calculated through the number density weighted averages of the specific heats of each of the major species. The k/\bar{m}_n in front of the source term is to relate the sources to the normalized temperature \mathcal{T} . The thermal energy source term is:

$$\begin{aligned} \mathcal{Q} = Q_{EUV} + Q_{NO} + Q_O + \frac{\partial}{\partial r} \left((\kappa_c + \kappa_{eddy}) \frac{\partial T}{\partial r} \right) \\ + N_e \frac{\bar{m}_i \bar{m}_n}{\bar{m}_i + \bar{m}_n} v_{in} (\mathbf{v} - \mathbf{u})^2, \end{aligned} \quad (17)$$

where $\kappa_c = 5.6 \times 10^{-4} T^{3/4}$ (in SI units) is the heat conductivity and κ_{eddy} is the heat conductivity due eddy diffusion. Q_{EUV} is the solar extreme ultraviolet heating, as described below. Q_{NO} and Q_O are cooling terms as described by Kockarts (1980), Kockarts and Peetermans (1970), and Roble et al. (1987). N_e is the electron density, \bar{m}_i and \bar{m}_n are the average mass of the ions and neutrals respectively, v_{in} is the ion-neutral collision frequency, and \mathbf{v} is the ion velocity. This term is the Joule (or frictional) heating caused by differences in the flows in the ions and neutrals (Rees, 1989; Schunk and Nagy, 2000), and includes the differences in each direction, instead of just the components orthogonal to the magnetic field.

GITM includes two models of solar irradiance: the Hinteregger et al. (1981) Solar EUV flux model (SERF1) and the Tobiska (1991) update to the Tobiska and Barth (1990) SERF2 model. These two models are based on the the daily average of $F_{10.7}$ and the 81 day mean of $F_{10.7}$. The

models have been modified to output the solar flux in 55 wavelengths that are then used in combination with the ionization and heating cross sections specified by Torr et al. (1979) to calculate the ionization rates and thermospheric and ionospheric heating. The Chapman integrals that are used to determine the intensity of the different solar wavelengths at a specified solar zenith angle and radial distance are approximated using formulation specified by Smith and Smith (1972). There is a heating efficiency that is included in the solar EUV heating. Stolarski (1976) describes a roughly constant solar EUV heating efficiency of approximately 0.35. Other studies have shown that the heating efficiency varies greatly with altitude and local time (Torr et al., 1980). For GITM, we decided to use an altitude-dependent heating efficiency that is close to the profiles described in Torr et al. (1980). This profile is shown in Fig. 3. This heating efficiency does not include the chemical heating that occurs due to exothermic reactions, as described by Schunk and Nagy (2000) and Rees (1989), which is also included in GITM.

We now turn to the equations of the horizontal dynamics. The horizontal continuity equation in

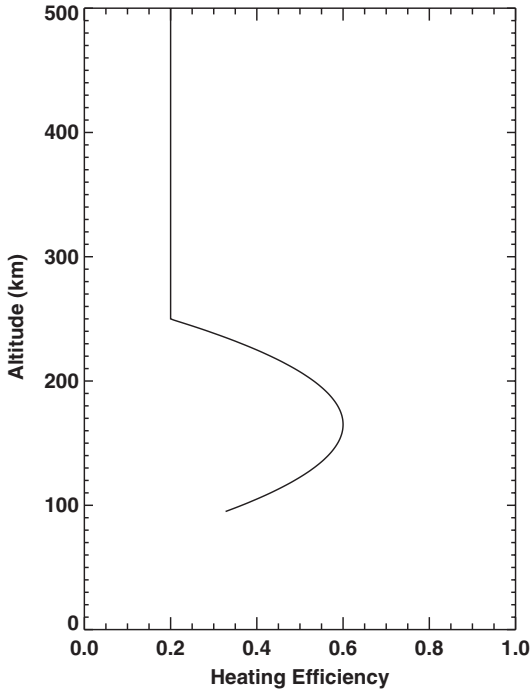


Fig. 3. The thermospheric efficiency for solar heating.

spherical coordinates is

$$\frac{\partial N_s}{\partial t} + N_s \left(\frac{1}{r} \frac{\partial u_\theta}{\partial \theta} + \frac{1}{r \cos \theta} \frac{\partial u_\phi}{\partial \phi} - \frac{u_\theta \tan \theta}{r} \right) + \frac{u_\theta}{r} \frac{\partial N_s}{\partial \theta} + \frac{u_\phi}{r \cos \theta} \frac{\partial N_s}{\partial \phi} = 0. \quad (18)$$

The eastward momentum equation becomes

$$\begin{aligned} \frac{\partial u_\phi}{\partial t} + u_r \frac{\partial u_\phi}{\partial r} + \frac{u_\theta}{r} \frac{\partial u_\phi}{\partial \theta} + \frac{u_\phi}{r \cos \theta} \frac{\partial u_\phi}{\partial \phi} \\ + \frac{1}{r \cos \theta} \frac{\partial \mathcal{F}}{\partial \phi} + \frac{\mathcal{F}}{r \rho \cos \theta} \frac{\partial \rho}{\partial \phi} \\ = \frac{\mathcal{F}_\phi}{\rho} + \frac{u_\phi u_\theta \tan \theta}{r} - \frac{u_r u_\phi}{r} \\ + 2\Omega u_\theta \sin \theta - 2\Omega u_r \cos \theta, \end{aligned} \quad (19)$$

where \mathcal{F}_ϕ is the force due to ion-neutral friction and viscosity in the ϕ direction. The last two terms are due to the Coriolis force.

The northward momentum equation becomes

$$\begin{aligned} \frac{\partial u_\theta}{\partial t} + u_r \frac{\partial u_\theta}{\partial r} + \frac{u_\theta}{r} \frac{\partial u_\theta}{\partial \theta} + \frac{u_\phi}{r \cos \theta} \frac{\partial u_\theta}{\partial \phi} \\ + \frac{1}{r} \frac{\partial \mathcal{F}}{\partial \theta} + \frac{\mathcal{F}}{r \rho} \frac{\partial \rho}{\partial \theta} \\ = \frac{\mathcal{F}_\theta}{\rho} - \frac{u_\phi^2 \tan \theta}{r} - \frac{u_\theta u_r}{r} \\ - \Omega^2 r \cos \theta \sin \theta - 2\Omega u_\phi \sin \theta. \end{aligned} \quad (20)$$

In the above two equations, the velocity terms on the right hand side are due to the spherical coordinates. The last two terms in this equation are the centrifugal and Coriolis forces. As before, all these terms vanish if there is no rotation and the horizontal wind is zero, and they cancel each other if the wind is exactly opposite to the rotation, i.e. $u_\phi = -r \cos \theta \Omega$.

The force terms due to ion-neutral friction and viscosity are

$$\begin{aligned} \mathcal{F}_\theta &= \rho_i v_{in} (v_\theta - u_\theta) + \frac{\partial}{\partial r} \eta \frac{\partial u_\theta}{\partial r}, \\ \mathcal{F}_\phi &= \rho_i v_{in} (v_\phi - u_\phi) + \frac{\partial}{\partial r} \eta \frac{\partial u_\phi}{\partial r}, \end{aligned} \quad (21)$$

where η is the coefficient of viscosity. Only the viscosity due to the radial shear of the horizontal wind is included. The first term on the right side is the ion drag.

The horizontal thermodynamic equation is

$$\frac{\partial \mathcal{T}}{\partial t} + \frac{u_\phi}{r \cos \theta} \frac{\partial \mathcal{T}}{\partial \phi} + \frac{u_\theta}{r} \frac{\partial \mathcal{T}}{\partial \theta} + (\gamma - 1) \mathcal{T} \times \left(\frac{1}{r} \frac{\partial u_\theta}{\partial \theta} + \frac{1}{r \cos \theta} \frac{\partial u_\phi}{\partial \phi} - \frac{u_\theta \tan \theta}{r} \right) = 0. \quad (22)$$

The thermal energy source terms are included in the vertical thermodynamic equation, described by Eq. (17).

2.2. Ion advection

The ion momentum equation can be written as

$$\rho_i \frac{d\mathbf{v}}{dt} = -\nabla(P_i + P_e) + \rho_i \mathbf{g} + eN_e(\mathbf{E} + \mathbf{v} \times \mathbf{B}) - \rho_i v_{in}(\mathbf{v} - \mathbf{u}), \quad (23)$$

where \mathbf{E} is the externally generated electric field (i.e. magnetospheric), \mathbf{B} is the magnetic field, N_e is the electron density, P_i and P_e are the ion and electron pressures, v_{in} is the ion-neutral collision frequency, e is the electron charge, and \mathbf{v} is the ion velocity. In GITM, we simplify the ion advection by assuming that the left-hand side is negligible relative to the other terms. Using this assumption, the ion momentum equation can be simplified to

$$\mathbf{v} = \frac{\mathbf{A}}{\rho_i v_{in}} + \frac{eN}{\rho_i v_{in}}(\mathbf{v} \times \mathbf{B}), \quad (24)$$

where

$$\mathbf{A} = \rho_i \mathbf{g} + eN_e \mathbf{E} - \nabla(P_i + P_e) + \rho_i v_{in} \mathbf{u}. \quad (25)$$

This can be solved to determine the ion velocity:

$$\mathbf{v} = \frac{\mathbf{A} \cdot \mathbf{b}}{\rho_i v_{in}} + \frac{\rho_i v_{in} \mathbf{A}_\perp + eN_e \mathbf{A}_\perp \times \mathbf{B}}{\rho_i^2 v_{in}^2 + e^2 N_e^2 B^2}, \quad (26)$$

where $B = |\mathbf{B}|$ is the magnitude of the magnetic field, $\mathbf{b} = \mathbf{B}/B$ is the direction of the magnetic field, and \mathbf{A}_\perp is the component of \mathbf{A} that is perpendicular to \mathbf{B} .

We examine two special cases of Eq. (26): (1) when there is only an external electric field, with no neutral winds, pressure gradients, or gravity; and (2) where there is only neutral winds and no electric field, pressure gradient, or gravity. For the first case, we take the limits as v_{in} becomes infinite (i.e. below 120 km altitude):

$$\mathbf{v} = \frac{eN_e}{\rho_i v_{in}} \mathbf{E} = 0, \quad (27)$$

and as v_{in} becomes close to zero (i.e. above 150 km altitude):

$$\mathbf{v} = \frac{\mathbf{E} \times \mathbf{B}}{B^2}. \quad (28)$$

The second case can be taken in the same limits, as v_{in} becomes infinite:

$$\mathbf{v} = \mathbf{u} \cdot \mathbf{b} + \mathbf{u}_\perp = \mathbf{u}, \quad (29)$$

and as v_{in} becomes close to zero:

$$\mathbf{v} = \mathbf{u} \cdot \mathbf{b} + \frac{m_i v_{in}}{eB} \mathbf{u}_\perp \times \mathbf{b} = \mathbf{u} \cdot \mathbf{b}, \quad (30)$$

given that $\rho_i = m_i N_e$.

The ion continuity equation is separated once again into horizontal

$$\frac{\partial N_j}{\partial t} + \frac{v_\theta}{r} \frac{\partial N_j}{\partial \theta} + \frac{v_\phi}{r \cos(\theta)} \frac{\partial N_j}{\partial \phi} = \mathcal{S}_j \quad (31)$$

and vertical

$$\frac{\partial \mathcal{N}_j}{\partial t} + v_r \frac{\partial \mathcal{N}_j}{\partial r} = 0 \quad (32)$$

directions. N_j is the number density of the j th ion, \mathcal{N}_j is $\ln(N_j)$, and \mathcal{S}_j is the total of the sources and losses of the ions due to chemistry and ionization. We can specify which ions we want to advect; while the other ion densities are controlled by chemical reactions. It is clear that O^+ is the most important species to advect, since it is the dominant ion in the low collision region of the ionosphere (Schunk and Nagy, 2000), so this is the only ion that is typically advected. It is possible to advect other species, simply by changing a single variable, which specifies the number of ion species to advect. The NCAR TIGCMs only advect O^+ also.

2.3. Chemistry

GITM contains chemistry between the ions and neutrals, ions and electrons, and neutral and neutrals. The primary source of ions on the dayside are due to the solar EUV



The cross sections for the above equations are specified by Torr et al. (1979). The chemistry within

GITM includes all of the chemical equations in Rees (1989). Alternatively, the chemical equations in Torr et al. (1979) can be used, although this does not appear to change the chemical makeup of the thermosphere and ionosphere tremendously.

Ion production rates due to auroral electron precipitation are derived from the formulation described by Frahm et al. (1997). Rees (1989) describes the partitioning of the electron precipitation ionization rates

$$P_{O^+} = 0.56P_A \frac{[O]}{0.92[N_2] + [O_2] + 0.56[O]}, \quad (39)$$

$$P_{O_2^+} = P_A \frac{[O_2]}{0.92[N_2] + [O_2] + 0.56[O]}, \quad (40)$$

$$P_{N_2^+} = 0.92P_A \frac{[N_2]}{0.92[N_2] + [O_2] + 0.56[O]}, \quad (41)$$

where P_A is the total ionization rate due to precipitating electrons, P_{O^+} , $P_{O_2^+}$, and $P_{N_2^+}$ are ionization rates for the individual species, and $[O]$, $[O_2]$, and $[N_2]$ are the number densities of atomic oxygen, molecular oxygen, and molecular nitrogen, respectively.

We use a grid-point dependent sub-cycling to calculate the chemistry within GITM. At altitudes below approximately 120 km, the time-step may be reduced to below 0.1 s, while above approximately 150 km, the time-step is not limited by chemistry, so full advection time-steps (2–4 s) can be taken. The sub-cycling allows the chemical dynamics to be closely investigated, so there is no assumption of local chemical equilibrium. For example, when an aurora arc starts, the formation of the E-region ionosphere can be examined.

2.4. Electron temperature calculation

If chemical reactions and viscous heating of the electron gas are neglected, the electron energy conservation equation becomes (Schunk and Nagy, 2000):

$$\begin{aligned} \frac{3}{2}k \frac{\partial N_e T_e}{\partial t} + \frac{3}{2}k N_e \mathbf{v}_e \cdot \nabla T_e \\ = -\frac{5}{2}N_e k T_e \nabla \cdot \mathbf{v}_e - \nabla \cdot \mathbf{q}_e + Q_e - L_e, \end{aligned} \quad (42)$$

where \mathbf{v}_e is the electron drift velocity, T_e is the electron temperature, \mathbf{q}_e is the electron heat flux, Q_e is the sum of the electron heat sources, while L_e is the sum of the electron heat losses. By using the

electron continuity equation:

$$\frac{\partial N_e}{\partial t} + \nabla \cdot (N_e \mathbf{v}_e) = 0, \quad (43)$$

the electron energy equation can be expressed in a more convenient form:

$$\begin{aligned} \frac{\partial T_e}{\partial t} = -\frac{2}{3}T_e \nabla \cdot \mathbf{v}_e - \mathbf{v}_e \cdot \nabla T_e \\ + \frac{2}{3N_e k} (-\nabla \cdot \mathbf{q}_e + Q_e - L_e). \end{aligned} \quad (44)$$

The first term on the right-hand side represents adiabatic expansion, the second term accounts for advection, the third term is the divergence of the electron heat flow vector, Q_e and L_e are the sum of all the heating and cooling rates, respectively.

The heat gained by the ambient electron gas from the photoelectrons and from super-elastic collisions with the neutrals acts to raise the electron temperature above the ion and neutral temperatures. The heating is due to solar EUV radiation, deactivation of excited neutral and ion species, energetic electron precipitation, Joule heating and so on. In GITM, we only take into account solar heating and Joule heating. Compared with Joule heating, solar heating is dominant except at high latitudes. The electron EUV heating is done in exactly the same way as the neutral EUV, but with a smaller heating efficiency (Stolarski, 1976).

A number of processes are effective in cooling the electron gas (Schunk and Nagy, 2000), and are included in GITM. In the lower F region, where the molecular species are abundant, rotational excitation of N_2 , $O_2(L(e, N_2)_{\text{rot}}, L(e, O_2)_{\text{rot}})$ and excitation of the fine structure levels of atomic oxygen ($L(e, O)_f$) are the most important cooling processes. At electron temperatures greater than 1500 K, vibrational excitation of N_2 , $O_2 (L(e, O_2)_{\text{vib}}, L(e, N_2)_{\text{vib}})$ and electronic excitation of $O(L(e, O(^1D)))$ have to be considered. At high altitudes, Coulomb collisions with the ambient ions ($L(e, i)$) are an important energy loss mechanism for thermal electrons (Schunk and Nagy, 1978).

In the collision dominated limit, the electron heat flux equation is

$$\mathbf{q}_e = -\beta_e \mathbf{J} - \kappa_e \nabla T_e, \quad (45)$$

where κ_e is the electron thermal conductivity in the limit of zero current. When the field-aligned currents are not present, the heat flux equation reduces to

$$\mathbf{q}_e = -\kappa_e \nabla T_e. \quad (46)$$

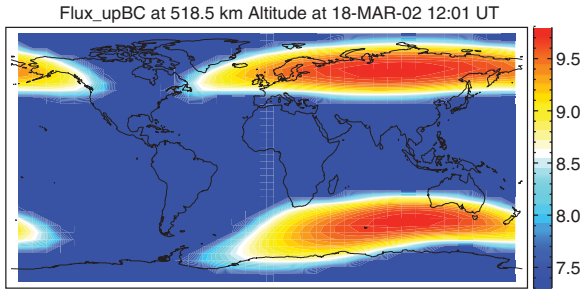


Fig. 4. The log of the energy input (in eV/cm²/s) at the top boundary for the electron temperature. The distribution of energy input is an oval in magnetic coordinates (magnetic latitude and magnetic local time), so the distortions are due to the mapping from the APEX magnetic coordinate system. This plot is similar to the heat flux specified by Liemohn et al. (2001).

An approximate expression for the electron thermal coefficient by using simple mean free path considerations is (Schunk and Nagy, 2000)

$$\kappa_e = \frac{7.7 \times 10^5 T_e^{5/2}}{1 + 3.22 \times 10^4 (T_e^2 / N_e) \sum_n N_n (q_D)_n}, \quad (47)$$

where the summation is over all the neutral species in the gas mixture and where $(q_D)_n$ is the Maxwellian-averaged momentum transfer cross section.

At the lower boundary, we set $T_e = T_n$. At the upper boundary (400–700 km), we use the equation

$$\frac{dT_e}{ds} = \frac{F_e}{\kappa_e}, \quad (48)$$

where F_e is the heat flow rate. We use a latitudinal profile of the magnetospheric heat flux as specified by Liemohn et al. (2001), shown in Fig. 4. From Fok et al. (1991) we set the energy deposition rates as a function of D_{st} , K_p and seasons.

3. Numerical schemes

This section describes the numerical schemes used in GITM to solve the equations presented in the previous section.

3.1. Spatial discretization for advection

The advection terms contain gradients and divergences of the primitive variables U . The spatial derivatives are obtained from finite differencing the face values

$$\nabla U_j = \frac{U_{j+1/2} - U_{j-1/2}}{\Delta x_j}, \quad (49)$$

where $j + 1/2$ is the cell interface between the cells indexed by j and $j + 1$ in the direction of gradient, and Δx_j is the cell size. The face values are taken as the average of the *left* and *right* face values U^L and U^R :

$$U_{j+1/2} = \frac{U_{j+1/2}^L + U_{j+1/2}^R}{2}. \quad (50)$$

We apply limited reconstruction (van Leer, 1979) to obtain the left and right face values

$$U_{j+1/2}^L = U_j + \frac{1}{2} \bar{\Delta} U_j, \quad (51)$$

$$U_{j+1/2}^R = U_{j+1} - \frac{1}{2} \bar{\Delta} U_j, \quad (52)$$

where $\bar{\Delta} U_j$ is the limited slope of the variable. We use a modified monotized central limiter. If the left and right slopes $\Delta U_{j-1/2} = U_j - U_{j-1}$ and $\Delta U_{j+1/2} = U_{j+1} - U_j$ have opposite signs, the limited slope is zero. Otherwise we take the

$$\bar{\Delta} U_j = \text{sgn} \Delta U_{j+1/2} \min(\beta |\Delta U_{j-1/2}|, \beta |\Delta U_{j+1/2}|, \frac{1}{2} |U_{j+1} - U_{j-1}|), \quad (53)$$

where sgn is the sign function, and $1 \leq \beta \leq 2$ is an adjustable parameter. We found that $\beta = 1.5$ produces robust and accurate results.

To make the numerical discretization stable, and to provide some upwind bias, we add a second-order Lax–Friedrichs numerical flux to the update. For example, in the vertical advection we add the gradient of the flux

$$F_{j+1/2} = \frac{1}{2} \max(c_{j-1/2}, c_{j+1/2}) (U_{j+1/2}^R - U_{j+1/2}^L), \quad (54)$$

where $c = |u| + c_s$ is the maximum wave speed calculated from the bulk speed u and the sound speed $c_s = \sqrt{\gamma p / \rho}$. For smooth regions the left and right face values are very close to each other and the diffusive flux is a second order term only. Where gradients vary sharply, the diffusive flux becomes first order, and it provides a stable and oscillation free solution.

3.2. Neutral friction, heat conduction, and viscosity

The neutral-neutral friction term, the heat conduction, and the viscosity terms are very stiff, therefore we use an implicit scheme for them. Since these terms are applied in the vertical direction only, the resulting linear systems require the inversion of simple tri-diagonal matrices. We apply a direct solver to obtain the solution. Note that when GITM is run on a parallel computer, the data is distributed

in the horizontal direction over the processors, so all data of the linear system is local.

3.3. Chemistry

The chemistry in GITM is solved for using a subcycling technique. This is more accurate than an implicit scheme and does not require any assumptions on chemical equilibrium. The subcycling is implemented on a grid-point by grid-point basis. For each iteration in the subcycle (or a chemical time-step), all sources and losses for all constituents are calculated. The time-step is then determined by enforcing that each species can only be reduced by a maximum of 25% in a single chemical time-step. If all species either increase in density or decrease by less than 25% in the advective time-step, then only 1 iteration is taken. If any species should decrease by more than 25% in the advective time-step, then multiple chemical time-steps are taken. Typically only a single step is needed above 150 km or so, while the chemical time-step is typically 0.001 s or less around 100 km altitude (i.e. approximately 2000 subcycling time-steps are taken). This makes the chemistry take approximately 20% of the computation time in a typical run.

4. Differences between GITM and TGCMs

The system of thermospheric advection equations are quite different than those specified by Dickinson et al. (1984) and Killeen and Roble (1984). There are two obvious differences: (1) GITM solves for a non-hydrostatic thermosphere, while the TGCMs force the thermosphere to be in hydrostatic equilibrium; and (2) Eqs. (16) and (22) include all of the divergence of the velocity terms, while the TGCMs contain some velocity divergence terms, but not all of them. For example, there is no $T\nabla \cdot \mathbf{u}$ in the temperature equation that is described by Killeen and Roble (1984). This term is the adiabatic heating and cooling due to the expansion or contraction of the atmosphere. In addition, the equations described by Killeen and Roble (1984) shows that there are possibly some terms in the conversion to spherical coordinates that are missing in the horizontal momentum equations in their study.

The benefit of a non-hydrostatic solution is clear when the vertical momentum equation is examined (Eq. (15)). There are a number of terms that can not be included when one assumes that gravity and the gradient in pressure are balanced: Coriolis, centri-

fugal acceleration, and ion drag to name three. In addition, the TGCMs assume that gravity is constant over the domain, while it actually varies from 9.5 at 100 km altitude to 8.0 at 700 km altitude. It would be extremely difficult to enforce a pure hydrostatic equilibrium on a pressure grid with varying gravity, since varying the height of the pressure grid would alter the gravity, and therefore the pressure balance. In addition to gravity, ion drag can be quite important in regions in which there is significant vertical ion velocities. For example, near the equator during storm times, the fountain effect could drag neutrals vertically. This can be quite important, since even small vertical motions can cause significant changes in the height profile of the thermosphere. The same is true in the throat region, where there is a small dip angle of the magnetic field. If the electric field becomes very large, a vertical $\mathbf{E} \times \mathbf{B}$ ion drift can result, creating a vertical neutral flow. Additionally, when the horizontal velocities become large, significant vertical flows can develop due to the Coriolis force. This would maximize near the equator, since the vertical Coriolis force contains a $\cos(\theta)$ term. While the neutral winds are typically small near the equator, during disturbed periods, propagating waves may bring strong neutral winds to the equatorial region, causing large vertical flows to develop.

Many other GCMs solve for mass mixing ratios, while GITM solves for the total number densities of the different constituents. The TGCMs solve for the mass mixing ratios (mmr) of O and O₂, then specify the mass mixing ratio (mmr) of N₂ as $1 - \text{mmr}(\text{O}) - \text{mmr}(\text{O}_2)$. This helps to ensure positivity in the solution and speeds up the calculation. While solving for mass mixing ratios is very similar to solving for the densities, as GITM does, GITM does not make the same assumption on N₂.

There are some numerical differences between GITM and other GCMs. For example, the NCAR TGCMs solve almost all of the equations using an implicit solver. We use an explicit solver that is limited to quite small time steps. For example, the TGCMs can typically take 5 min time steps, while GITM takes an approximately 2 s time step. This time step is the result of having very tight resolution near the lower boundary of the model and resolving the sound speed in this region. While this makes the GITM run much slower than the TGCMs, GITM is a parallel code that can break the problem onto many processors, thereby gaining

some of the run-time back. The run-time is also strongly controlled by the number of grid cells in the vertical and horizontal directions. Typically, GITM runs 3 times faster than real-time on 32 processors using the same resolution as the NCAR TGCMs.

GITM's ion momentum equations (23) and (26) are different than the NCAR TIGCMs ion momentum equation: the NCAR models do not contain the gradient in pressure crossed with \mathbf{B} term, the $\mathbf{g} \times \mathbf{B}$ term, or any of the terms containing \mathbf{u} . The \mathbf{u}_\perp term

is taken into account through the use of an electric field. This electric field is expressed as the solution to a potential Poisson equation, where the source term is the field-line integrated divergence of the conductivity weighted neutral winds (e.g. Ridley et al., 2003). This type of solution insures that the magnetic field lines are all equipotentials. These models only do this at low-latitudes, though, so it is assumed that the neutral wind forcing (of the ion velocity) is minimal at high-latitudes.

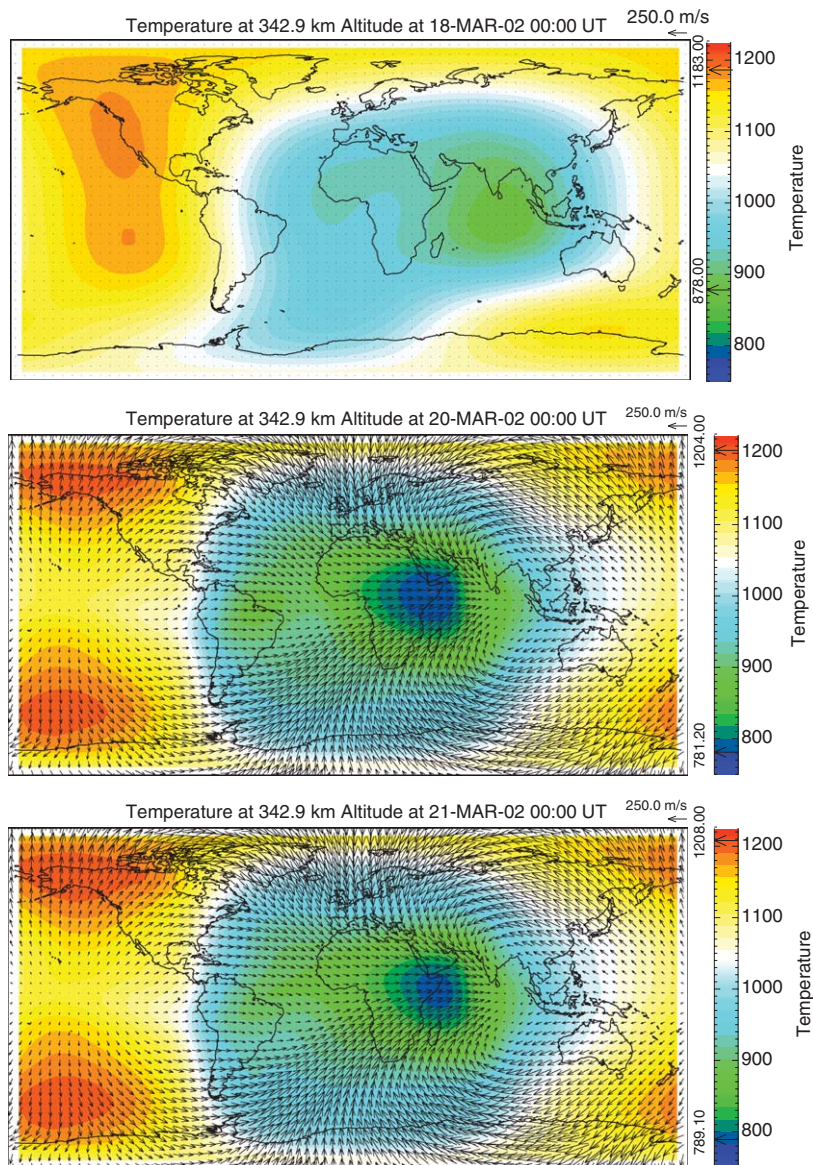


Fig. 5. The temperature (in Kelvin) of the thermosphere at 343 km altitude for March 18, 20, and 21. The code was initialized with MSIS on March 18, so the top figure shows the MSIS results. The bottom 2 figures show the GITM results for midnight on March 20 and 21. The black arrows show the neutral wind velocity.

The neutral-ion coupling dynamics within GITM is correct in the E-region, in which there is significant drag by the neutrals. The E-region is where a dynamo electric field, driven by the drag on the neutrals, is generated. Without significant conductivity, an electric potential applied perpendicular to a magnetic field will stay constant along that field. Above the E-region, the conductivity drops off quickly, so dynamo electric fields created in the E-region map up to the F-region and above (see, for example, Ridley et al., 2003). The actual calculation and mapping of the electric field is not calculated within GITM. It is only the ion velocity that is calculated.

Because GITM does not include a mapped dynamo electric field, there is essentially no equatorial fountain effect. This could be fixed by adding an empirical low-latitude electric field model, or adding a self-consistent electric field calculation, as is done in the TIEGCM and CTIP. The self-consistent electric field is actually calculated when GITM is run as part of the Space Weather Modeling Framework (Tóth et al., 2005), but the electrodynamic solver is currently not included in the stand-alone version of GITM.

5. Test results

In this section, we describe two simulations that illustrate how GITM models the thermosphere and ionosphere during equinox and solstice conditions. The runs are compared to MSIS and IRI results. A separate paper will demonstrate how GITM compares with measurements and other model results of the high-latitude neutral winds (Deng and Ridley, 2006). For each simulation, the $F_{10.7}$ value is held at 150, while the IMF B_z is set to +2 nT. The hemispheric power index is at a very low value (2 GW) for the entire period. These conditions reduce the influence of the high-latitude inputs, which are typically quite dynamic. The IGRF magnetic field for the starting date is used.

Each simulation is initiated using MSIS and IRI and run for three days. We show the initial time, and snap shots after two and three days into the simulation. Comparison of the results after two and three days demonstrate that GITM produces a stable diurnally varying solution. Comparison with MSIS/IRI initial conditions checks whether GITM provides a reasonable solution. For each of the simulations, the code was run at the same horizontal resolution that the NCAR TIEGCM is typically run

at: 5° latitude by 5° longitude. The altitude resolution was set to approximately 0.3 of a scale-height on the dayside.

The final simulation shows how GITM can run in 1-D. This run is the same as the equinox 3-D run, so the model results can be directly compared.

5.1. Equinox simulation

Fig. 5 shows the simulation results for March 18, 20, and 21. The dayside maximum temperature in GITM is 1207 K, while the maximum in MSIS is 1183 K, a 2% difference. The minimum temperature is 11% lower in GITM than in MSIS. The location of the peak temperatures in GITM is a little more poleward and westward than the peaks in MSIS, while the minimum temperature in GITM is a little more westward than in MSIS. Interestingly, GITM shows a small midnight temperature maximum, which has been observed from ground-based Fabry–Pérot interferometers (Faivre et al., 2005). Fig. 6 shows a local time profile of the temperature at 343 km altitude at the equator. There is a clear secondary maximum in the temperature at 22:45 local time.

Fig. 7 shows a latitudinal cut of the temperature from MSIS and GITM near noon. These cuts show that the high-latitude temperature maxima

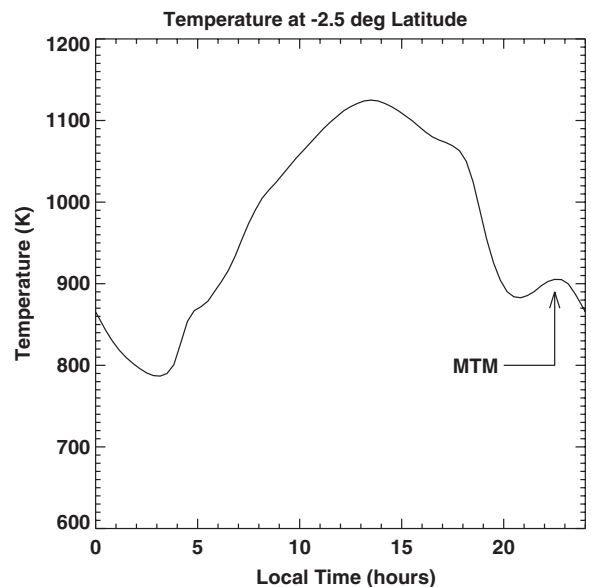


Fig. 6. The temperature at -2.5° latitude as a function of local time at 343 km altitude, with a small midnight temperature maximum (MTM).

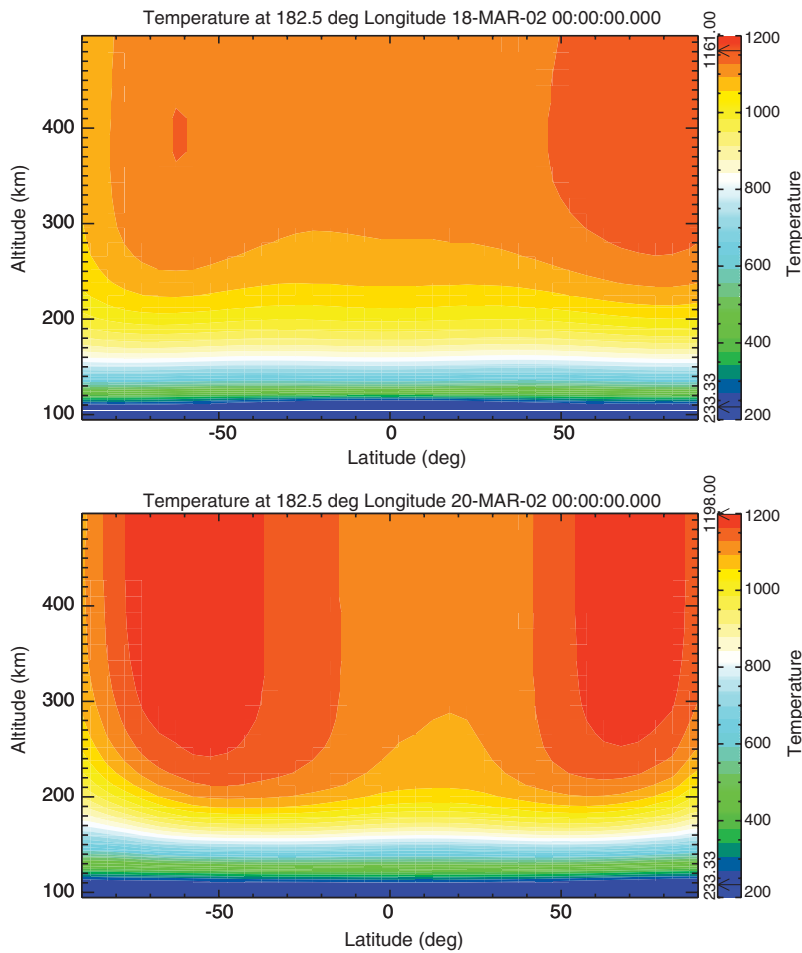


Fig. 7. A latitudinal cut (at 182° longitude) of the temperature of the thermosphere (in Kelvin) derived from MSIS (top) and GITM (bottom) for March 18 and 20, respectively.

are reproduced in GITM, although the maximum is 2.9% higher in GITM than in MSIS. The locations of the maxima (in this plane) in GITM are almost identical to the locations in MSIS. GITM reproduces the minimum in temperature near the equator. There is a decrease in the temperature at the poles in GITM that is not as strong in MSIS.

Another difference between GITM and MSIS is that GITM is much more symmetric between the northern and southern hemisphere. This can be seen in both Figs. 5 and 7. We do not understand the reason for the asymmetry in MSIS, while the symmetry in GITM is caused by uniform heating between the hemispheres by sunlight.

The electron density structure in GITM does not reproduce all of the features that are present in IRI,

as shown in Fig. 8. Namely, GITM produces a single peak in electron density at the equator, while IRI has two peaks slightly off the equator. The reason for this is that GITM does not contain a self-consistent equatorial electric field, so there is no upward ion flow in the F-region at the equator, causing a down-welling at higher latitudes. Instead, all of the electron density is centered at the equator. It is clear that without adding an equatorial electrojet electric field, the low-latitude dynamics in GITM is incorrect. In addition, the peak electron density in GITM is a bit lower than in IRI.

Fig. 9 shows the electron density and ion convection velocity from IRI (top) and GITM (bottom) for 112 km altitude. The electron densities on the dayside are very similar, with GITM having a slightly higher maximum density. On the

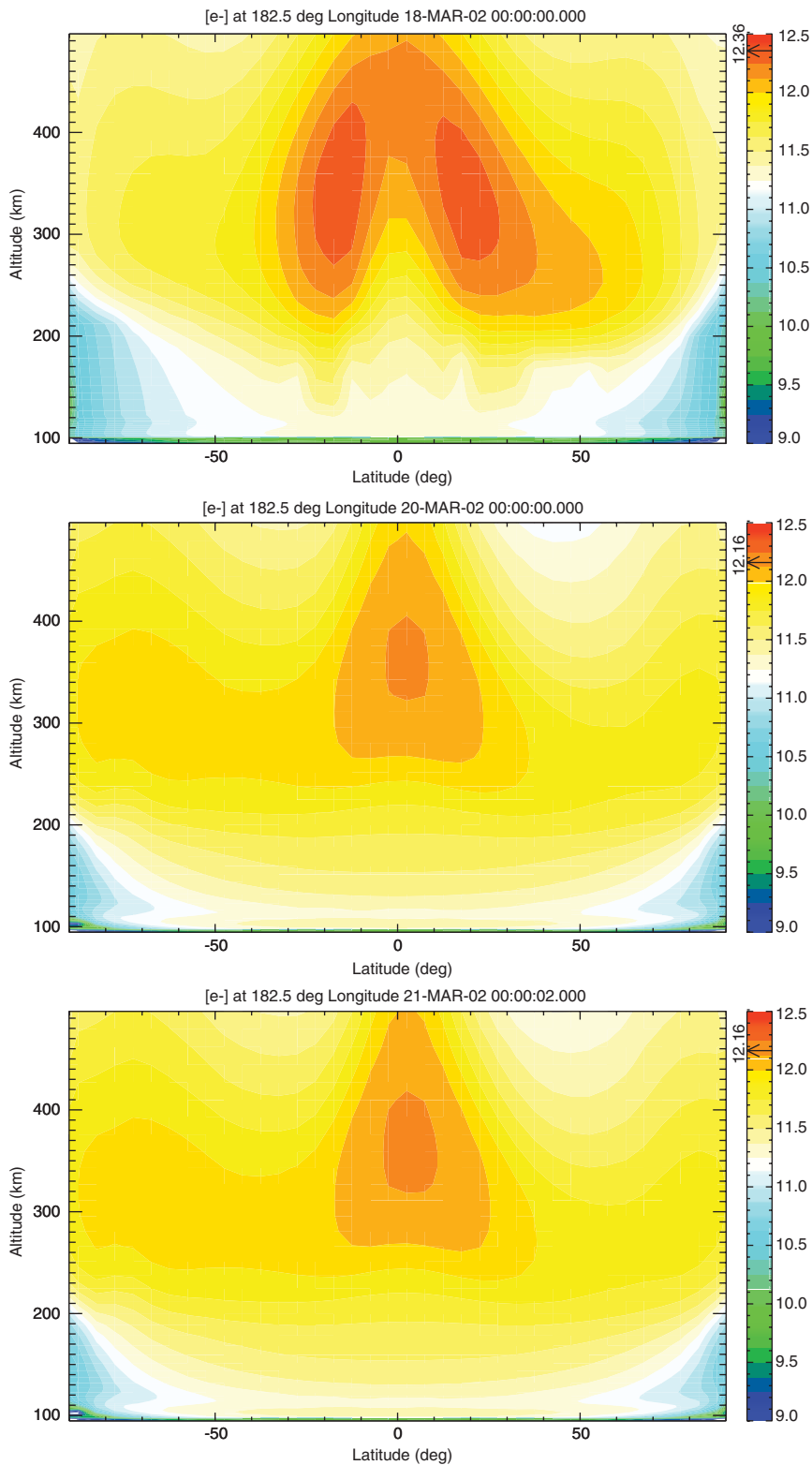


Fig. 8. The electron density (in m^{-3}) from IRI (top) and GITM (middle and bottom) for March 18, 20, and 21. These plots show latitudinal slices of the electron density near noon (i.e. 180° longitude). The log of the electron density is shown.

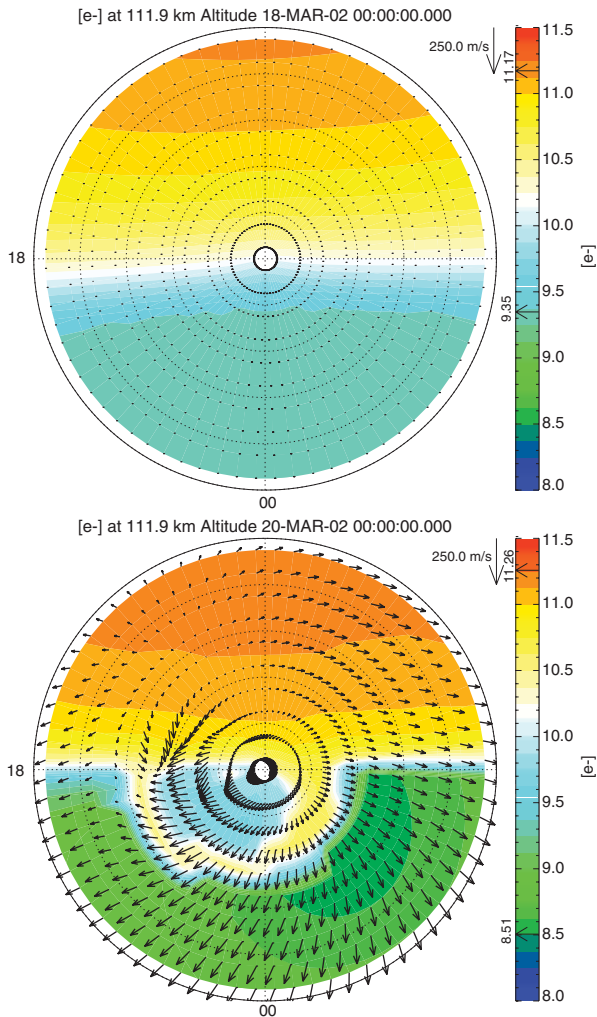


Fig. 9. The IRI (top) and GITM (bottom) electron density over the northern polar region at 112 km altitude with the horizontal ion convection velocity over-plotted. The outer circle is 40° latitude, while each circle represents 10° latitude. Noon is at the top of each plot, while dusk is to the left. The log of the electron density (in m^{-3}) is shown.

nightside, there are stark differences—GITM produces an auroral oval, where IRI does not have an oval, and GITM shows the electron density to be almost an order of magnitude less than the IRI density. In GITM, the decrease in the E-region density is caused by rapid recombination that takes place after sunset. GITM does not include a starlight or geocoronal source of ionization, so the nightside densities may be much lower than expected. At this low altitude, the ion convection velocities are driven primarily by the neutral wind drag, so there is a flow roughly from day to night,

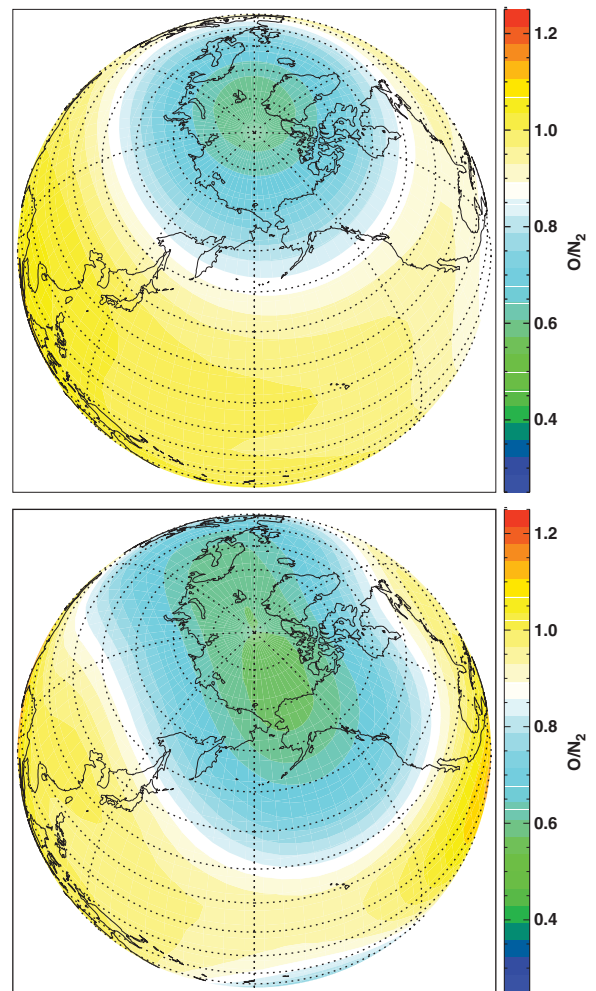


Fig. 10. The integrated O/N_2 ratio for MSIS (top) and GITM (bottom). The integrated O/N_2 ratio was determined by integrating the N_2 and O densities downward from the top of the model until the N_2 integral reached 10^{21} particles/ m^2 . Sunward is out of the page, while dusk is to the right.

although the tidal forcing (at the lower boundary) causes the flow to be directed towards dawn and dusk also, as is expected at this altitude.

The integrated O/N_2 ratio, shown in Fig. 10 is determined by starting at the top of the model, integrating both N_2 and O until the integral of N_2 becomes 10^{21} particles/ m^2 , then taking the ratio of the two integrals. The top plot shows the MSIS results, while the bottom plot shows the GITM results. The view-point is looking at noon. The GITM results show that the O/N_2 ratio is slightly lower than the MSIS results. In addition, the polar

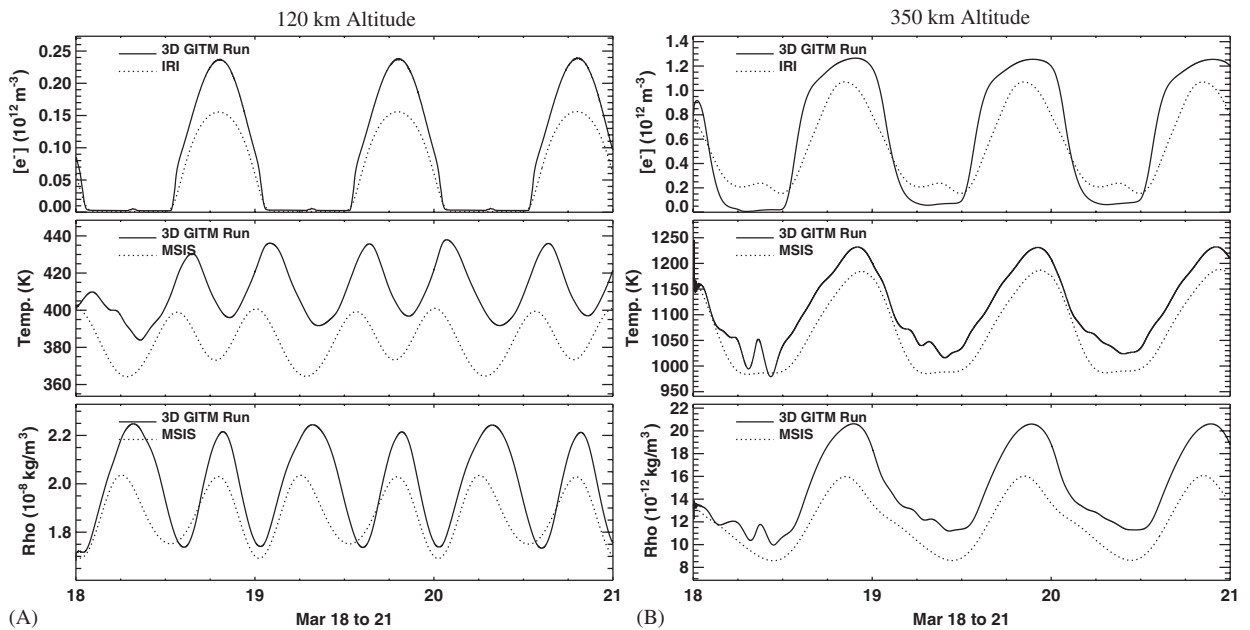


Fig. 11. A comparison of the 3-D GITM (solid lines) electron density (top), temperature (middle), and mass density (bottom) at 120 km (left) and 350 km (right) altitude above Boulder, CO (254.75° longitude, 40.02° latitude) to MSIS and IRI (dotted lines).

hole of O/N₂ is slightly larger in GITM, extending to lower latitudes both at noon and near midnight.

Fig. 11 shows a time-history of the GITM and MSIS/IRI results at a single latitude and longitude and two altitudes (120 and 350 km). At low altitudes, the GITM electron density is 60% larger than the IRI densities at noon. On average, the temperature in GITM is 8% larger than MSIS, and shows similar but phase-shifted (by approximately 3 h) temperature oscillations. The neutral mass densities in GITM and MSIS are very similar, with almost identical minimum values and frequency, but with GITM having slightly large maximum values. At high altitudes, the agreement is better. The average electron density is almost identical between GITM and IRI, the temperatures are within 4% of each other, with GITM being larger, and the mass density difference is within the daily variation of each.

Fig. 12 shows a time-history of two different 3-D GITM simulations, one with using MSIS and IRI as the initial conditions, as it typically done, and one using the values from MSIS and IRI at the equator at midnight for each grid cell as the initial condition. The second run therefore started with no gradients in latitude and longitude, but with vertical gradients. Fig. 12 shows how the two different runs start

out different, but eventually the two simulations begin to match each other.

In the lower thermosphere and ionosphere this happens quite quickly. Because the lower ionosphere is driven strongly by rapid chemical reactions, the two simulations are barely different right from the beginning. The temperature difference is only a 5 K for the first 18 h, and then the temperatures are the same.

In the upper thermosphere and ionosphere, the runs are different for longer, but they have similar reactions to the initial conditions. For example, at 09 UT on March 18, both simulations show a large wave in the temperature and density. This is repeated on the 19th, but at a much lower amplitude. On the 20th, there is no wave structure. This is most likely caused by strong neutral winds advecting dispersing the initial condition. The time of the increase is near local midnight, so this might be a region of convergent flows, which would cause adiabatic heating and an increase in the density. As the initial condition is completely wiped out of the simulation, the strong neutral winds die down and the convergent flow eases. In the first 2 h of the simulation (Fig. 13), there is significant sound wave activity as the atmosphere attempts to find a vertical equilibrium. In the normal run, the large vertical

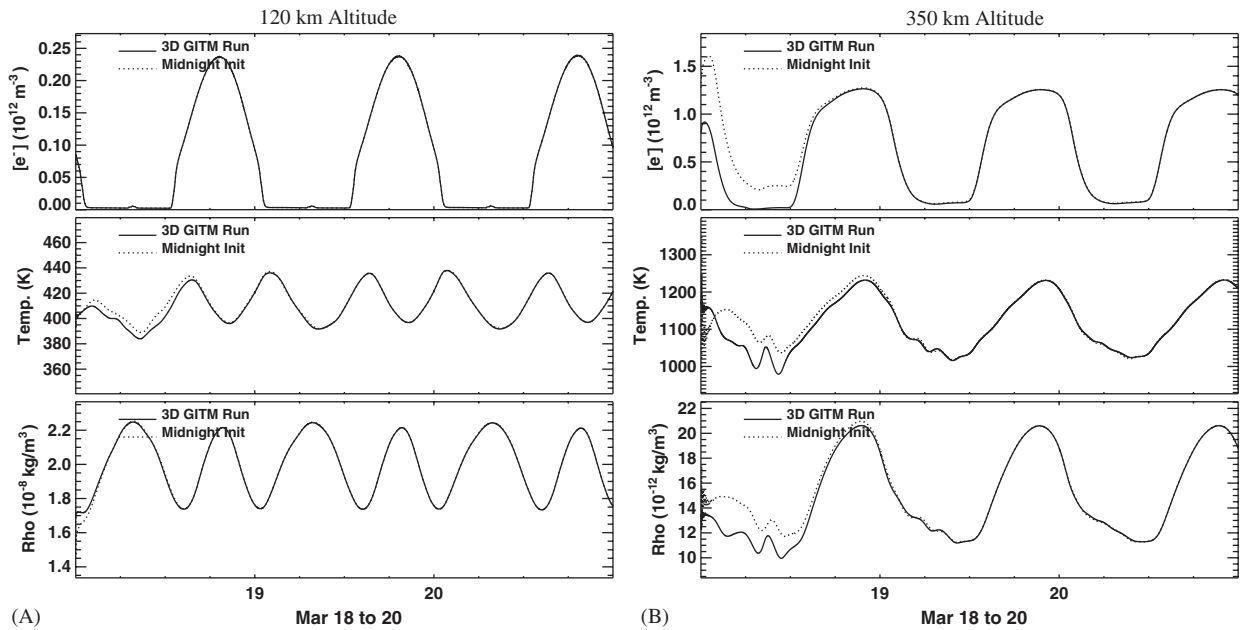


Fig. 12. A comparison of the 3-D GITM results initiated with MSIS and IRI (solid) and initiated with uniform horizontal values (dashed) in the same format as Fig. 11.

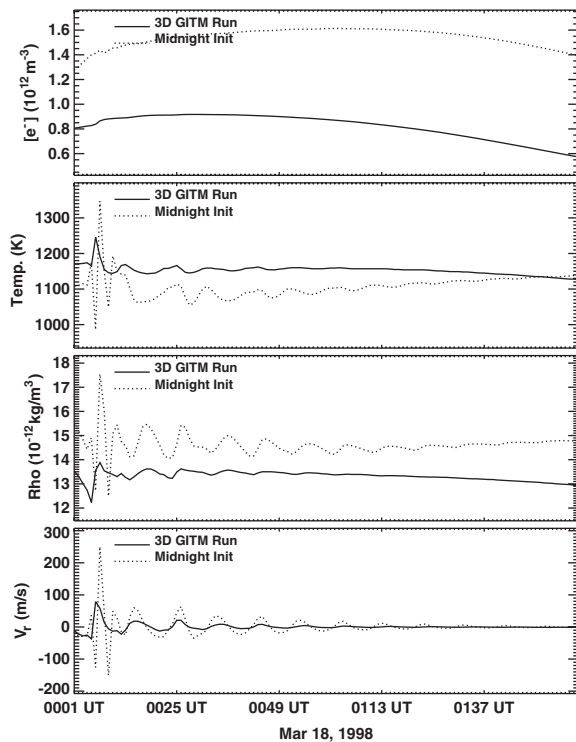


Fig. 13. A comparison of the 3-D GITM results at 350 km altitude initiated with MSIS and IRI (solid) and initiated with uniform horizontal values (dashed) in a similar format as Fig. 12. The bottom plot, in this case, is the radial neutral velocity. In addition, only the first 2 h of the simulation are shown.

wave flows die out after approximately 45 min, while the run that is further out of equilibrium shows strong vertical flows for the first hour and a half.

5.2. Northern summer solstice simulation

For this simulation, we initiated GITM using MSIS and IRI on June 18, and ran through June 21. Fig. 14 shows the temperature structure at 336 km altitude for June 18, 20, and 21 at 00 UT. The top plot is therefore the MSIS results, while the bottom two plots show GITM results 24 h apart. Once again, the solution shows a diurnally reproducible solution. GITM shows a maximum temperature that is 2% larger than the MSIS results while the minimum temperature is 1.2% smaller than MSIS. The location of the maxima is very similar in the GITM and MSIS result, although GITM shows a secondary maxima in the southern hemisphere, which is not indicated in the MSIS results. MSIS shows two minima, while GITM shows a single minimum near midnight close to the equator. The main difference between GITM and MSIS is that GITM shows a warmer winter pole, by almost 100 K.

Fig. 15 shows that GITM produces a small midnight temperature maximum in the solstice case as well as the equinox case. There is a ridge of

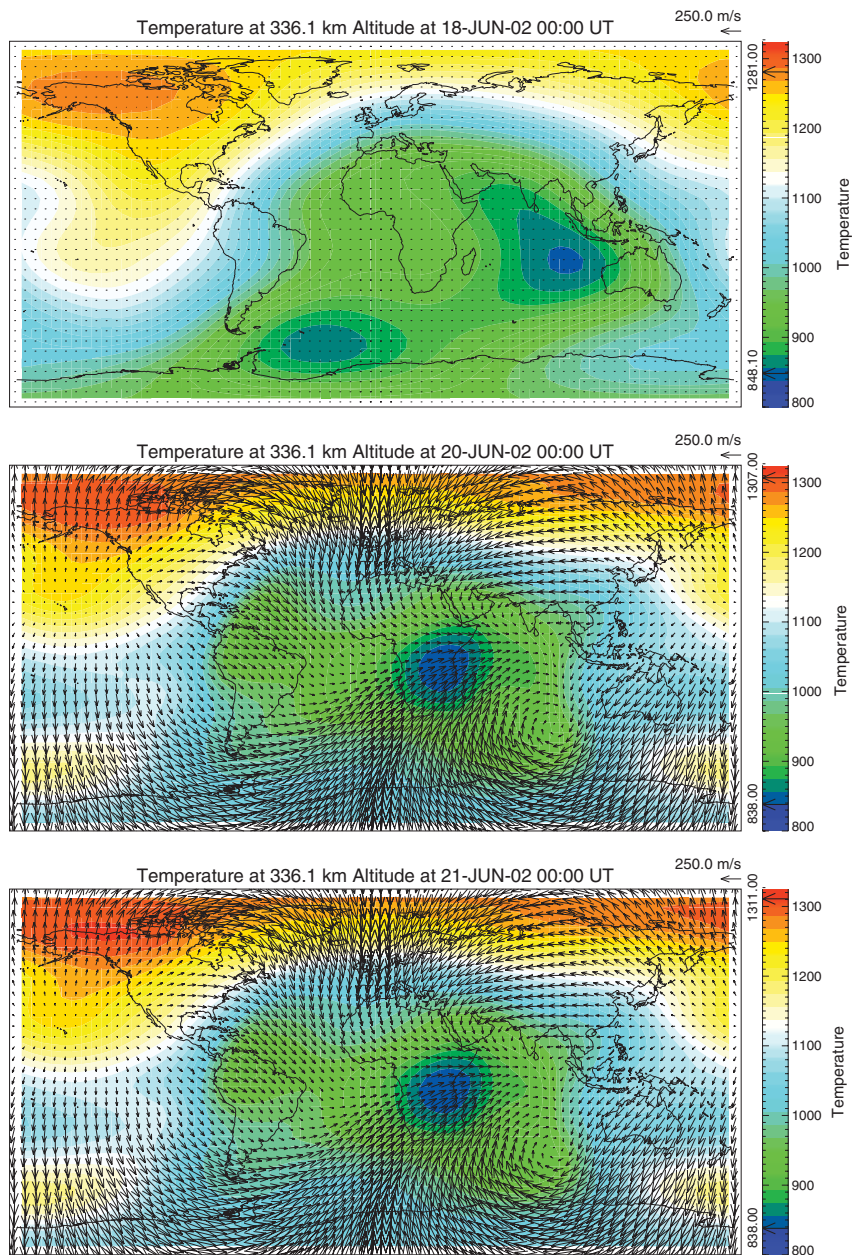


Fig. 14. Same as Fig. 5, but for June 18, 20, and 21.

slightly higher temperatures that extends along the eastern coast of South America up to the western edge of Africa. This ridge is in approximately the same location that the southward directed flow from the northern hemisphere meets the northward directed flow from the southern hemisphere. This means that there is a convergence of flow in this

region, causing adiabatic heating of the thermosphere.

There is once again a large difference between the structure of the electron density in GITM and IRI (Fig. 16). The main difference is once again caused by the lack of an electric field. GITM does show a stronger bifurcation of the electron

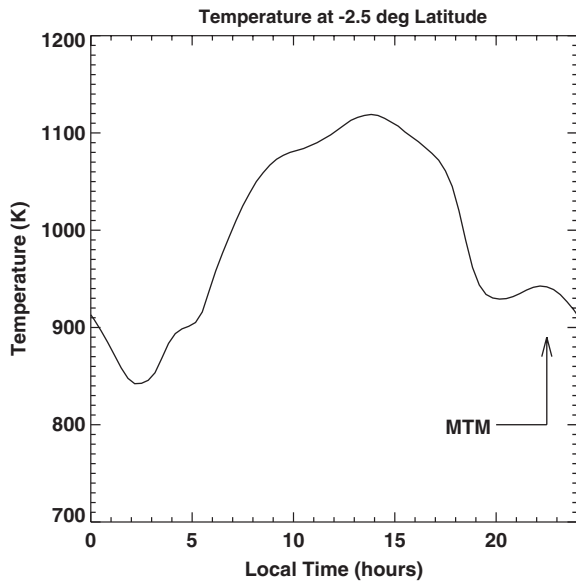


Fig. 15. Same as Fig. 6, but for solstice conditions.

density at 250 km or so compared to the equinox conditions, but it is not nearly as strong as the IRI results. GITM also produces a minimum in the electron density above 400 km altitude at mid- to low-latitudes in the southern (winter) hemisphere, with another minimum at the pole. This is not observed in the IRI results. Another difference is in the E-region in the winter hemisphere—GITM produces a larger electron density by a couple orders of magnitude. This is most likely caused by soft electron precipitation (i.e. polar rain) causing some ionization in the polar cap. The northern (summer) hemisphere results are very comparable between GITM and IRI: the F-region peak location and value are very comparable. In the winter hemisphere, the F-region peak is similar in location.

Fig. 17 shows the O/N₂ ratio for MSIS and GITM. Once again, the GITM obtains a slightly reduced O/N₂ ratio, and the “hole” expanding to slightly lower latitudes at noon. The minimum value in GITM is only slightly lower than the MSIS results, while the values near the equator are quite comparable between the models.

5.3. 1-D simulation

Fig. 18 shows the ability of GITM to run as a 1-D model of the coupled ionosphere-thermosphere as

well as a 3-D model. The same simulation was carried out for March 18–21, as shown in Fig. 11 with the code configured to run in 1-D above Boulder, CO. Because the 3-D model results were extracted at this exact location, the 1-D and 3-D results can be directly compared.

At low altitudes the electron density is a little lower (20%) in the 1-D result than the 3-D result between 10 and 18 local time. At high altitudes, the electron density is larger in the 1-D model than the 3-D model during these times. Therefore, the lower electron density at low altitudes could be due to a greater loss of solar EUV above 120 km altitude in the 1-D model. The mass density is almost identical between the simulations, showing clear tidal structures. Because all tides except the diurnal tidal component are caused by horizontal convergence and divergence of flows, and those are not present within the 1-D model, this semi-diurnal tide must be directly propagating up from the boundary condition, which does have a semi-diurnal tide. Interestingly, the temperature in the 1-D simulation only shows a diurnal tide, while the 3-D simulation shows a strong semi-diurnal tidal component. This shows that the temperature wave structure is most likely maintained through the horizontal winds rather than the vertical motion.

At high altitudes, the electron density between the 1-D and 3-D results are very similar, even though the temperature and density structure are very different between the 1-D and 3-D results. The day-night gradient in the density and temperature in the 3-D model is minimized by horizontal neutral winds. Because the 1-D model does not have these horizontal pressure gradient driven winds, the gradient can become much larger.

There are some significant advantages of running in 1-D—namely the simplification of the dynamics and a dramatic decrease in run-time. For example, the 3-D model result presented in Figs. 11 took 7.1 h on 32 processors, while the 1-D calculation took 11 min on a single desktop computer. There are number of reasons for this: (a) there are 2592 times less cells to consider between a 5° by 5° calculation and a 1-D calculation; (b) ignoring the horizontal advection reduces the amount of calculations the model has to do during each time-step by almost a factor of two; (c) because the time-step is limited by the smallest grid cells, the longitudinally small cells near the pole may limit the time-step in the 3-D calculation; and (d) at the end of each time-step in

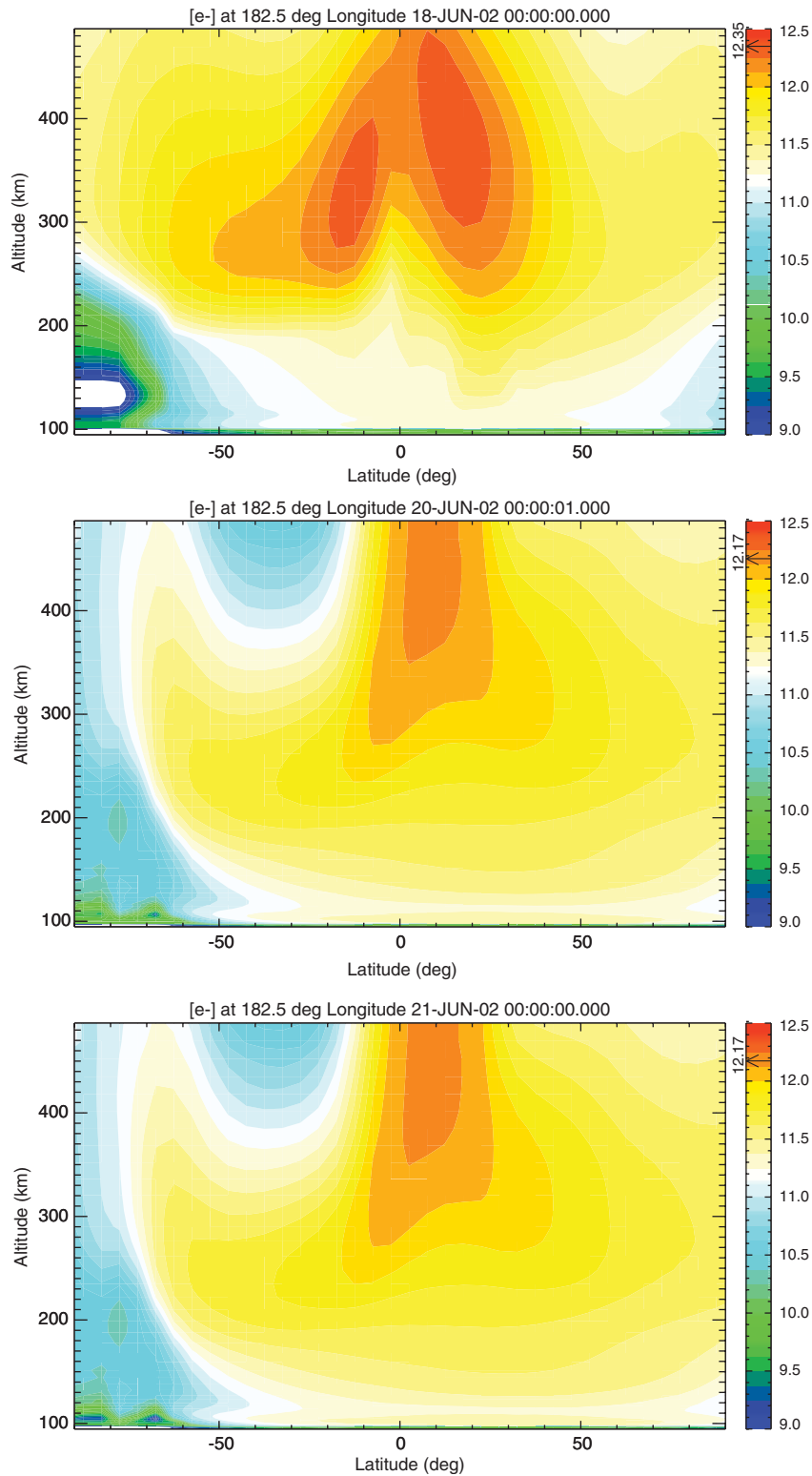


Fig. 16. Same as Fig. 8, but for June 18, 20, and 21. Note that the electron density obtained by IRI in the winter polar region between 120 and 150 km becomes much lower than the minimum in the color bar, so it saturates.

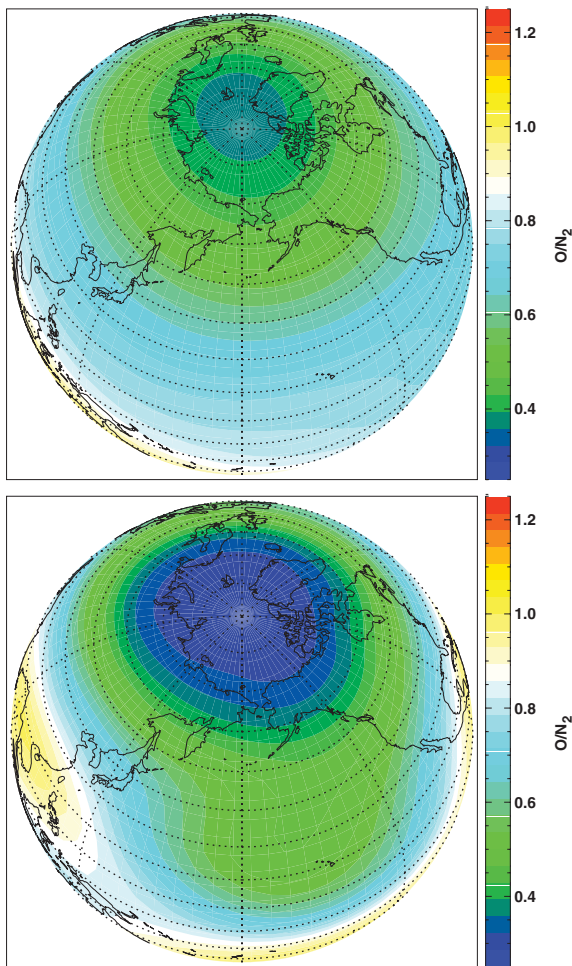


Fig. 17. Same as Fig. 10 but for solstice conditions.

the 3-D simulation the blocks must message-pass information to neighboring blocks, meaning that each block must wait for the slowest block, which is always the blocks near dusk, because of sub-cycling in the chemistry due to the large losses. In 3-D, the speed of the code is always limited by the chemistry in the dusk sector, while in 1-D, the code speeds up dramatically at sunrise and slows down at sunset.

The speed of the 1-D calculation makes it much easier to test new physics and to debug the model. It is also easy to run long time periods to test the stability of the model over weeks. It is clear, though, that there are significant differences between the 1-D and 3-D calculations, so modeling of real events is typically done with the 3-D model.

6. Summary

In this paper a new global ionosphere–thermosphere model (GITM) has been presented. GITM is a three-dimensional, parallel, spherical code that models the Earth’s thermosphere and ionosphere system using a stretched altitude grid. The model allows for non-hydrostatic solutions, resolving sound and gravity waves. GITM explicitly considers the neutral densities of O, O₂, N(²D), N(²P), N(⁴S), N₂, NO, H, and He; and ion species O⁺(⁴S), O⁺(²D), O⁺(²P), O₂⁺, N⁺, N₂⁺, NO⁺, H⁺, and He⁺. In addition, GITM self-consistently solves for the neutral, ion, and electron temperature; the bulk horizontal neutral winds; the vertical velocity of the individual species; and the ion and electron velocities. At the core, GITM separates the vertical and horizontal advection and uses the logarithm of number density in the vertical solver to numerically ease the exponential fall-off of the atmosphere.

We show two 3-D simulations: an equinox case and a solstice case, and compare the results to MSIS and IRI. GITM reproduces the temperature structure of the thermosphere reasonably well, having maxima and minima near 350 km within 3% of MSIS values. The general temperature distribution is similar to the MSIS results also, although there are some differences.

The electron densities in GITM are found to be comparable in magnitude with IRI, but the equatorial fountain effect is missing. This is because there is no equatorial electric field specified in the code at this time. During equinox conditions, GITM and IRI match at higher latitudes quite well in the F-region, but GITM produces a much lower E-region nightside electron density. GITM further has an aurora oval. During solstice conditions, the location and magnitude of the F-region peak is similar at mid-latitude and at high latitude in the summer hemisphere. In the winter hemisphere, the F-region peak in GITM is too low compared to IRI.

The study by Deng and Ridley (2006) focuses on comparing the neutral winds produced by GITM to previous measurement and modeling studies. This study examines the response of the high-latitude neutral winds to a wide variety of interplanetary magnetic field levels, solar EUV driving levels, and auroral input levels. The neutral wind results from GITM are in very good agreement with ground-based measurements, satellite-based measurements, and other modeling results of the neutral winds.

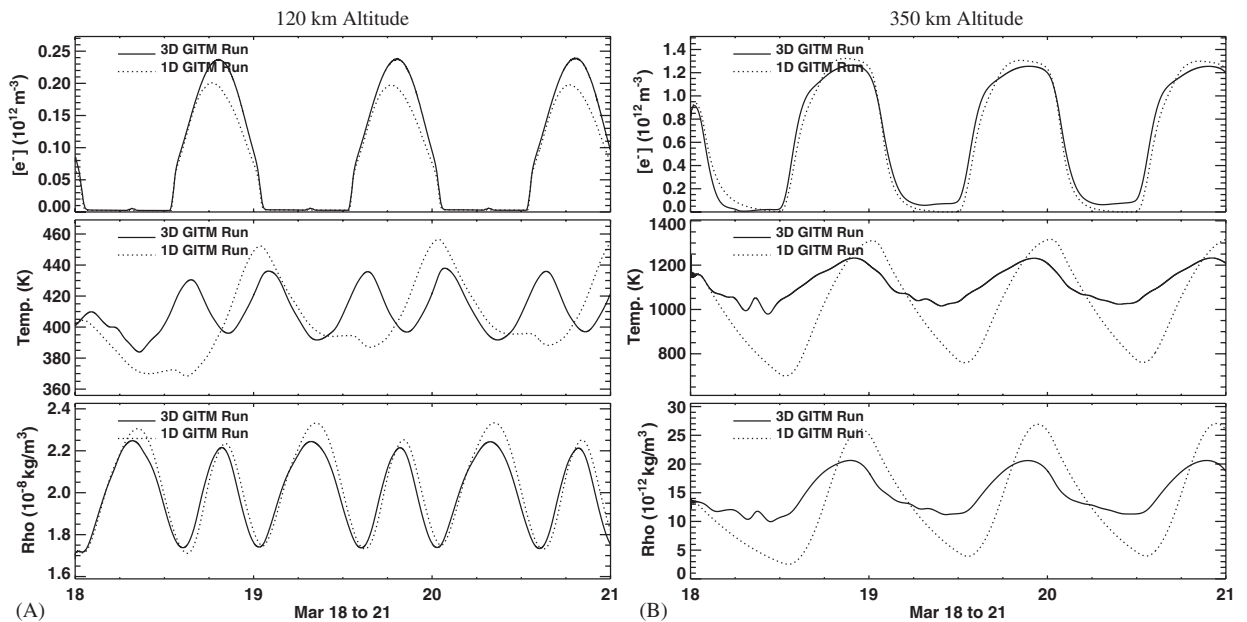


Fig. 18. A comparison of the 3-D GITM (solid) results and 1-D GITM results (dashed) in the same format as Fig. 11.

Acknowledgments

This research was supported by NSF through grants ATM-0077555 and ATM-0417839, the DoD MURI program grant F4960-01-1-0359, and NASA grant NNG04GK18G. GT was partially supported by the Hungarian Science Foundation (OTKA grants T047042 and T037548).

References

- Bilitza, D., 2001. International reference ionosphere 2000. *Radio Science* 36, 261.
- Colegrove, F., Johnson, F., Hanson, W., 1966. Atmospheric composition in the lower thermosphere. *Journal of Geophysical Research* 71, 2227.
- Deng, Y., Ridley, A., 2006. Dependence of neutral winds on convection E-field, solar EUV and auroral particle precipitation at high latitudes. *Journal of Geophysical Research*, in press.
- Dickinson, R., Ridley, E., Roble, R., 1981. A three-dimensional, time-dependent general circulation model of the thermosphere. *Journal of Geophysical Research* 86, 1499.
- Dickinson, R., Ridley, E., Roble, R., 1984. Thermospheric general circulation with coupled dynamics and composition. *Journal of Atmospheric Science* 41, 205.
- Faivre, M., Meriwether, J., Fese, C., Biondi, M., 2005. Climatology of the midnight temperature maximum phenomenon at Arequipa, Peru. *Journal of Geophysical Research* 110, submitted for publication.
- Fok, M.-C., Kozyra, J., Brace, L., 1991. Solar cycle variations in the subauroral electron temperature enhancement: comparison of AE-C and DE 2 satellite observations. *Journal of Geophysical Research* 96, 1861.
- Foster, J., 1983. An empirical electric field model derived from Chatanika radar data. *Journal of Geophysical Research* 90, 981.
- Frahm, R., Winningham, J., Sharber, J.R., Link, R., Crowley, G., Gaines, E.E., Chenette, D.L., Anderson, B.J., Potemra, T.A., 1997. The diffuse aurora: a significant source of ionization in the middle atmosphere. *Journal of Geophysical Research* 102, 28203.
- Fuller-Rowell, T., Evans, D., 1987. Height-integrated Pedersen and Hall conductivity patterns inferred from TIROS-NOAA satellite data. *Journal of Geophysical Research* 92, 7606.
- Fuller-Rowell, T., Rees, D., 1980. A three-dimensional, time-dependent, global model of the thermosphere. *Journal of Atmospheric Science* 37, 2545.
- Fuller-Rowell, T., Rees, D., 1983. Derivation of a conservative equation for mean molecular weight for a two constituent gas within a three-dimensional, time-dependent model of the thermosphere. *Planetary Space Science* 31, 1209.
- Hardy, D., Gussenhoven, M., Raistrick, R., McNeil, W., 1987. Statistical and functional representation of the pattern of auroral energy flux, number flux, and conductivity. *Journal of Geophysical Research* 92, 12275.
- Harris, M.J., Arnold, N.F., Aylward, A.D., 2002. A study into the effect of the diurnal tide on the structure of the background mesosphere and thermosphere using the new coupled middle atmosphere and thermosphere (cmat) general circulation model. *Annals of Geophysics* 20, 225.
- Hedin, A., 1983. A revised thermospheric model based on mass spectrometer and incoherent scatter data: MSIS-83. *Journal of Geophysical Research* 88, 10170.
- Hedin, A., 1987. MSIS-86 thermospheric model. *Journal of Geophysical Research* 92, 4649.

- Hedin, A., 1991. Extension of the MSIS thermosphere model into the middle and lower atmosphere. *Journal of Geophysical Research* 96, 1159.
- Heelis, R., Lowell, J., Spiro, R., 1982. A model of the high-latitude ionospheric convection pattern. *Journal of Geophysical Research* 87, 6339.
- Heppner, J., Maynard, N., 1987. Empirical high-latitude electric field models. *Journal of Geophysical Research* 92, 4467.
- Hinteregger, H., Fukui, K., Gibson, B., 1981. Observational, reference and model data on solar EUV from measurements on AE-E. *Geophysics Research Letters* 8, 1147.
- Killeen, T., Roble, R., 1984. An analysis of the high-latitude thermospheric wind pattern calculated by a thermospheric general circulation model 1. Momentum forcing. *Journal of Geophysical Research* 89, 7509.
- Kockarts, G., 1980. Nitric oxide cooling in the terrestrial thermosphere. *Geophysics Research Letters* 7, 137.
- Kockarts, G., Peetermans, W., 1970. Atomic oxygen infrared emission in the Earth's upper atmosphere. *Planetary Space Science* 18, 271.
- Liemohn, M.W., Kozyra, J.U., Thomsen, M.F., Roeder, J.L., Lu, G., Borovsky, J.E., Cayton, T.E., 2001. The dominant role of the asymmetric ring current in producing the stormtime D_{st} . *Journal of Geophysical Research* 106, 10883.
- Meyer, C., 1999. Gravity wave interactions with mesospheric planetary waves: a mechanism for penetration into the thermosphere-ionosphere system. *Journal of Geophysical Research* 104, 28181.
- Oehmke, R., 2004. High performance dynamic array structures. Ph.D. thesis, University of Michigan, Department of Electrical Engineering and Computer Science.
- Oehmke, R., Stout, Q., 2001. Parallel adaptive blocks on the sphere. In: *Proceedings of the 11th SIAM Conference Parallel Processing for Scientific Computing*. SIAM, Philadelphia, PA.
- Powell, K., Roe, P., Linde, T., Gombosi, T., De Zeeuw, D.L., 1999. A solution-adaptive upwind scheme for ideal magnetohydrodynamics. *Journal of Computational Physics* 154, 284.
- Rawer, K., Bilitza, D., Ramakrishnan, S., 1978. Goals and status of the international reference ionosphere. *Reviews in Geophysics* 16, 177.
- Rees, D., 1989. *Physics and chemistry of the upper atmosphere*. Cambridge University Press, New York, NY 10022, USA.
- Rees, D., Fuller-Rowell, T., 1988. Understanding the transport of atomic oxygen in the thermosphere using a numerical global thermospheric model. *Planetary Space Science* 36, 935.
- Rees, D., Fuller-Rowell, T., 1990. Numerical simulations of the seasonal/latitudinal variations of atomic oxygen and nitric oxide in the lower thermosphere and mesosphere. *Advanced Space Research* 10 (6), 83–102.
- Richmond, A., 1992. Assimilative mapping of ionospheric electrodynamics. *Advanced Space Research* 12, 59.
- Richmond, A., 1995. Ionospheric electrodynamics using magnetic apex coordinates. *Journal of Geomagnetism and Geoelectricity* 47, 191.
- Richmond, A., Kamide, Y., 1988. Mapping electrodynamic features of the high-latitude ionosphere from localized observations: technique. *Journal of Geophysical Research* 93, 5741.
- Richmond, A., Roble, R., 1987. Electrodynamical effects of thermospheric winds from the NCAR thermospheric general circulation model. *Journal of Geophysical Research* 92, 12365.
- Richmond, A., Ridley, E., Roble, R., 1992. A thermosphere/ionosphere general circulation model with coupled electrodynamics. *Geophysics Research Letters* 19, 369.
- Ridley, A., Crowley, G., Freitas, C., 2000. An empirical model of the ionospheric electric potential. *Geophysics Research Letters* 27, 3675.
- Ridley, A., Gombosi, T., De Zeeuw, D.L., Clauer, C., Richmond, A., 2003. Ionospheric control of the magnetospheric configuration: neutral winds. *Journal of Geophysical Research* 108, 2002JA009464.
- Roble, R., Ridley, E., 1987. An auroral model for the NCAR thermospheric general circulation model (TGCM). *Annals of Geophysics* 5A, 369.
- Roble, R., Ridley, E., 1994. A thermosphere-ionosphere-mesosphere-electrodynamics general circulation model (time-gcm): equinox solar cycle minimum simulations (300–500 km). *Geophysics Research Letters* 21, 417.
- Roble, R., Ridley, E., Dickinson, R., 1987. On the global mean structure of the thermosphere. *Journal of Geophysical Research* 92, 8745.
- Roble, R., Ridley, E., Richmond, A., Dickinson, R., 1988. A coupled thermosphere/ionosphere general circulation model. *Geophysics Research Letters* 15, 1325.
- Schunk, R., Nagy, A., 1978. Electron temperatures in the f -region of the ionosphere. *Reviews in Geophysics and Space Physics* 16, 355.
- Schunk, R., Nagy, A., 2000. *Ionospheres*. Cambridge Press, Cambridge University.
- Schunk, R.W., Scherliess, L., Sojka, J.J., Thompson, D.C., Anderson, D.N., Codrescu, M., Minter, C., Fuller-Rowell, T.J., Heelis, R.A., Hairston, M., Howe, B.M., 2004. Global assimilation of ionospheric measurements (GAIM). *Radio Science* 39, doi:10.1029/2002RS002794.
- Smith, F.I., Smith, C., 1972. Numerical evaluation of Chapman's grazing incidence integral $ch(x;\chi)$. *Journal of Geophysical Research* 77, 3592.
- Stolarski, R., 1976. Energetics of the midlatitude thermosphere. *Journal of Atmospheric and Terrestrial Physics* 38, 863.
- Tobiska, W., 1991. Revised solar extreme ultraviolet flux model. *Journal of Atmospheric and Terrestrial Physics* 53, 1005.
- Tobiska, W., Barth, C., 1990. A solar EUV flux model. *Journal of Geophysical Research* 95, 8243.
- Torr, D., Torr, M., Brinton, H., Brace, L., Spencer, N., Hedin, A., Hanson, W., Hoffman, J., Nier, A., Walker, J., Rusch, D., 1979. An experimental and theoretical study of the mean diurnal variation of O^+ , NO^+ , O_2^+ , and N_2^+ ions in the mid-latitude F_1 layer of the ionosphere. *Journal of Geophysical Research* 84, 3360.
- Torr, M., Richards, P., Torr, D., 1980. A new determination of the ultraviolet heating efficiency. *Journal of Geophysical Research* 85 (A12), 6819.
- Tóth, G., Sokolov, I.V., Gombosi, T.I., Chesney, D.R., Clauer, C., Zeeuw, D.L.D., Hansen, K.C., Kane, K.J., Manchester, W.B., Powell, K.G., Ridley, A.J., Roussev, I.I., Stout, Q.F., Volberg, O., Wolf, R.A., Sazykin, S., Chan, A., Yu, B., Kóta, J., 2005. Space weather modeling framework: A new tool for the space science community. *Journal of Geophysical Research* 110, A12226, doi:10.1029/2005J-A011126.

- van Leer, B., 1979. Towards the ultimate conservative difference scheme, V: a second order sequel to Godunov's method. *Journal of Computational Physics* 32, 101.
- Wang, W., Killeen, T., Burns, A., Roble, R., 1999. A high-resolution, three-dimensional, time-dependent nested grid model of the coupled thermosphere-ionosphere. *Journal of Atmospheric and Terrestrial Physics* 61, 385.
- Wang, W., Killeen, T., Burns, A., Reinisch, B., 2001. A real-time model-observation comparison of f_2 peak electron densities during the Upper Atmospheric Research Collaboratory campaign of October 1997. *Journal of Geophysical Research* 106, 21077.
- Weimer, D., 1996. A flexible, IMF dependent model of high-latitude electric potential having space weather applications. *Geophysics Research Letters* 23, 2549.